The Astrophysical Journal, 780:25 (19pp), 2014 January 1 doi:10.1088/0004-637X/780/1/25

MODELING SELF-SUBTRACTION IN ANGULAR DIFFERENTIAL IMAGING: APPLICATION TO THE HD 32297 DEBRIS DISK

Thomas M. Esposito[1], Michael P. Fitzgerald[1], James R. Graham[2], and Paul Kalas[2]
[1] Department of Physics and Astronomy, 430 Portola Plaza, University of California, Los Angeles, CA 90095-1547, USA; esposito@astro.ucla.edu
[2] Astronomy Department, B-20 Hearst Field Annex 3411, University of California, Berkeley, CA 94720-3411, USA
Received 2013 June 21; accepted 2013 October 17; published 2013 December 10

ABSTRACT

We present a new technique for forward-modeling self-subtraction of spatially extended emission in observations processed with angular differential imaging (ADI) algorithms. High-contrast direct imaging of circumstellar disks is limited by quasi-static speckle noise, and ADI is commonly used to suppress those speckles. However, the application of ADI can result in self-subtraction of the disk signal due to the disk's finite spatial extent. This signal attenuation varies with radial separation and biases measurements of the disk's surface brightness, thereby compromising inferences regarding the physical processes responsible for the dust distribution. To compensate for this attenuation, we forward model the disk structure and compute the form of the self-subtraction function at each separation. As a proof of concept, we apply our method to 1.6 and 2.2 μm Keck adaptive optics NIRC2 scattered-light observations of the HD 32297 debris disk reduced using a variant of the "locally optimized combination of images" algorithm. We are able to recover disk surface brightness that was otherwise lost to self-subtraction and produce simplified models of the brightness distribution as it appears with and without self-subtraction. From the latter models, we extract radial profiles for the disk's brightness, width, midplane position, and color that are unbiased by self-subtraction. Our analysis of these measurements indicates a break in the brightness profile power law at $r \approx 110$ AU and a disk width that increases with separation from the star. We also verify disk curvature that displaces the midplane by up to 30 AU toward the northwest relative to a straight fiducial midplane.

Key words: circumstellar matter – infrared: planetary systems – stars: individual (HD 32297) – techniques: high angular resolution – techniques: image processing

Online-only material: color figures

1. INTRODUCTION

Debris disks produced by mutual collisions of orbiting planetesimals are known to exist around several hundred nearby main-sequence stars (see, e.g., Wyatt 2008 and references therein). The dust in these systems can be detected through scattered starlight or thermal emission, offering a view of the circumstellar environment during planet formation. Circumstellar debris disks represent the final stages of the planet formation process (Wyatt 2008). Moreover, the presence of a debris disk can be seen as an indicator of planet formation. For example, many directly imaged extrasolar planets observed to date around main-sequence stars are located in systems with substantial debris disks (e.g., β Pictoris, Fomalhaut, and HR 8799; Lagrange et al. 2010; Kalas et al. 2008; Marois et al. 2010b). Morphological structures in the disk can act as signposts of planets that interact with the dust and planetesimals present (e.g., Mouillet et al. 1997; Heap et al. 2000; Wyatt 2003; Kalas et al. 2005; Quillen 2006; Ertel et al. 2012; Thebault et al. 2012 and references therein). These structures can also provide information about the mechanisms that replenish the dust and sculpt its distribution.

Measurements of dust-scattered light can probe the location, abundance, size, composition, and structure (i.e., porosity) of dust grains in the disk. Consequently, scattered light is sensitive to disk structure. However, measuring scattered light is difficult because, although coronagraphs can be used to block light from the star, residual wavefront aberrations scatter starlight such that the faint disk signal is often overwhelmed. These aberrations are time-dependent, further complicating their removal. While adaptive optics (AO) corrects for rapidly varying atmospheric speckles, longer timescale changes in the wave aberrations preclude simple schemes for stellar point-spread function (PSF) calibration. Fewer than 20 debris disks have been spatially resolved in scattered light since the first example was imaged in the β Pic system (Smith & Terrile 1984), although the majority of these systems were resolved within the last decade due to advances in high-contrast imaging technology and methods.

Angular differential imaging (ADI; Mueller & Weigelt 1987; Marois et al. 2006) has proven to be an effective means for self-calibration of the time-variable residual stellar PSF. Higher contrast can be achieved by combining ADI with the method of Lafrenière et al. (2007) for constructing reference PSFs through a locally optimized combination of images (LOCI). Ground-based ADI observations on an altitude–azimuth mounted telescope require the science camera to track the telescope pupil such that in the focal plane, the PSF orientation remains fixed but the field of view (FOV) rotates throughout the exposure sequence. For a given exposure in the sequence, one can then use other exposures to build a reference PSF that is well suited to removing the stellar PSF. The LOCI algorithm refines construction of the reference PSF by assembling it in subsections to minimize the PSF subtraction residuals locally rather than globally. This technique has proved effective for ground-based detections of planets (Marois et al. 2008, 2010b; Lagrange et al. 2010; Bonnefoy et al. 2011, 2013; Currie et al. 2011, 2012a; Galicher et al. 2011; Skemer et al. 2012; Brandt et al. 2013; Carson et al. 2013; Delorme et al. 2013) and circumstellar disks (Buenzli et al. 2010; Thalmann et al. 2010, 2011, 2013; Lagrange et al. 2012; Milli et al. 2012; Rodigas et al. 2012).

The exclusion of images near in time from the pool used in reference PSF construction largely mitigates the conflation

of point-source PSFs with the residual stellar PSF. However, this task becomes more difficult for extended sources such as disks because they subtend a larger angle and therefore require greater time separation. If the necessary images are not excluded and the extended-source PSF is blended with the residual stellar PSF, then some or all of the source's flux is removed during PSF subtraction (Milli et al. 2012). For a given on-sky brightness distribution, this "self-subtraction" is a function of radial separation, azimuthal angle, and the ADI/LOCI parameters.

One way around the issue of self-subtraction is to use a different observational or data reduction method, although each strategy has its drawbacks. Using a reference PSF from a diskless star will avoid removing the disk flux, but it also usually offers inferior speckle suppression, because the speckle pattern changes with stellar spectral type and instrumental flexure from changes in telescope orientation. Spectral differential imaging (e.g., Smith 1987; Racine et al. 1999; Vigan et al. 2010) uses the invariance of the stellar PSF in simultaneous images at multiple wavelengths to differentiate it from the disk, but this method commonly requires specific spectral features in the target and instruments capable of making these observations. Polarimetric differential imaging (e.g., Kuhn et al. 2001; Perrin et al. 2004; Quanz et al. 2011) separates the polarized light of the disk from the unpolarized starlight but requires an instrument with polarimetry capabilities and relatively bright targets. Recently, principal component analysis (PCA; Amara & Quanz 2012; Quanz et al. 2013; Thalmann et al. 2013) and related algorithms such as Karhunen–Loéve image projection (Soummer et al. 2012) have come into use as alternatives to, or in conjunction with, ADI/LOCI. These algorithms are effective and provide a nice complement to ADI/LOCI, but they can also cause self-subtraction if the set of reference images is not carefully selected to omit modes equal to those of the target object in the region being optimized.

It is also possible to reduce self-subtraction by tuning the parameters of the ADI/LOCI algorithm to perform a "conservative" PSF subtraction (Buenzli et al. 2010; Thalmann et al. 2010, 2011, 2013; Boccaletti et al. 2012; Currie et al. 2012b; Lagrange et al. 2012; Rodigas et al. 2012). These tempered implementations often have the downside of poorer noise attenuation than more aggressive formulations as a result of lower correlation between the reference PSF and the residual stellar PSF in the data. In addition, less aggressive reductions do not see in as close to the star for a given ADI sequence, thus limiting investigation of the system's inner regions, where planets are most likely to reside. Efforts have also been made to systematically characterize the biases introduced into brightness distributions by ADI/LOCI processing and adapt the algorithms to minimize those biases (Marois et al. 2010a; Milli et al. 2012).

In this paper, we present a different approach to reducing the effects of self-subtraction, with a new technique for forward modeling the amount of self-subtraction of extended emission in ADI-processed images. We test the effectiveness and validity of our technique on Keck AO NIRC2 imaging of the HD 32297 debris disk at 1.6 and 2.2 μm. HD 32297 is an A star located at a distance of 112^{+15}_{-12} pc (Perryman et al. 1997). Its circumstellar disk has been observed at wavelengths ranging from the optical through the millimeter regime and displays interesting morphological features, including brightness asymmetries and a warp. This disk is a useful test case because it is bright and has reference star-subtracted *Hubble Space Telescope* (*HST*) imaging at similar wavelengths (albeit at lower spatial resolution) to our own observations (Schneider et al. 2005; Debes et al. 2009). In addition, the wealth of previous observations gives us many points of comparison for our work (Kalas 2005; Fitzgerald et al. 2007; Moerchen et al. 2007; Redfield 2007; Maness et al. 2008; Mawet et al. 2009; Boccaletti et al. 2012; Currie et al. 2012b; Donaldson et al. 2013).

We describe our self-subtraction modeling routine in Section 2. We present details of our observations, our data reduction methods, and the results of our application of self-subtraction modeling to the HD 32297 debris disk in Section 3. Finally, we discuss the fidelity and robustness of our modeling and the implications of our results in Section 4 and then summarize our conclusions in Section 5.

2. A NEW TECHNIQUE FOR MODELING ADI SELF-SUBTRACTION

Our technique for modeling the effects of self-subtraction in ADI is based on the operations that a modified LOCI algorithm performs on the images in a data set to subtract the stellar PSF and speckle noise. We can use the technique to inspect where self-subtraction effects make the greatest impact. The method can also be used as a tool for comparing the LOCI-processed observations with models of the disk surface brightness derived from three-dimensional dust distribution models.

Here we derive the self-subtraction model for the case in which the data are acquired with ADI. For simplicity, we assume that each exposure in the data set is short enough that no blurring due to field rotation occurs, although this effect could be included with a simple modification to the algorithm. Moreover, we do not account for off-axis coronagraphic PSF variation.

The ADI target exposures from which the stellar PSF is to be subtracted compose the sequence T_i. Let $g(r, \phi)$ be the scene on the sky (e.g., the disk), which depends on the distance from the host star r and the position angle (P.A.) ϕ measured counterclockwise from north in the sky reference frame. Actual images will also contain contributions from the star due to imperfect on-axis PSF suppression, but because the subtraction algorithm's operations are linear, we can consider the effects of the star on the rest of the scene independently. Therefore, we can define T_i in terms of the scene g as

$$T_i(r, \theta) = g(r, \theta - \theta_i) = g(r, \theta) \otimes \delta(\theta_i), \quad (1)$$

where θ is the angle measured counterclockwise from north in the detector reference frame (i.e., the detector vertical) and θ_i is the P.A. of the image T_i in the detector frame. In the following steps, we define T_i using the first equality. We only include the second to illustrate that assuming infinitesimal exposure times allows us to express T_i as the scene convolved with a delta function located at θ_i.

The reference PSF constructed for $T_i(r, \theta)$ is a linear combination of all target images weighted by their associated LOCI coefficients $c_{ij}(r, \theta)$, which the LOCI algorithm computes when trying to minimize the residuals in each subsection. Our notation differs slightly from LOCI convention here, in that j ranges over all images. This requires c_{ij} to be zero when an image T_j is excluded from the reference PSF for target image T_i, i.e., when $i = j$ or when $|\theta_j - \theta_i|$ is less than a minimum rotation threshold set by the LOCI parameters (see Figure 1). In addition, c_{ij} is a function of both r and θ by convention, but here we force it to be a function of only r by taking the median over all optimization subsections at a given radius. This modification makes the modeling more tractable because we need only divide T_i into

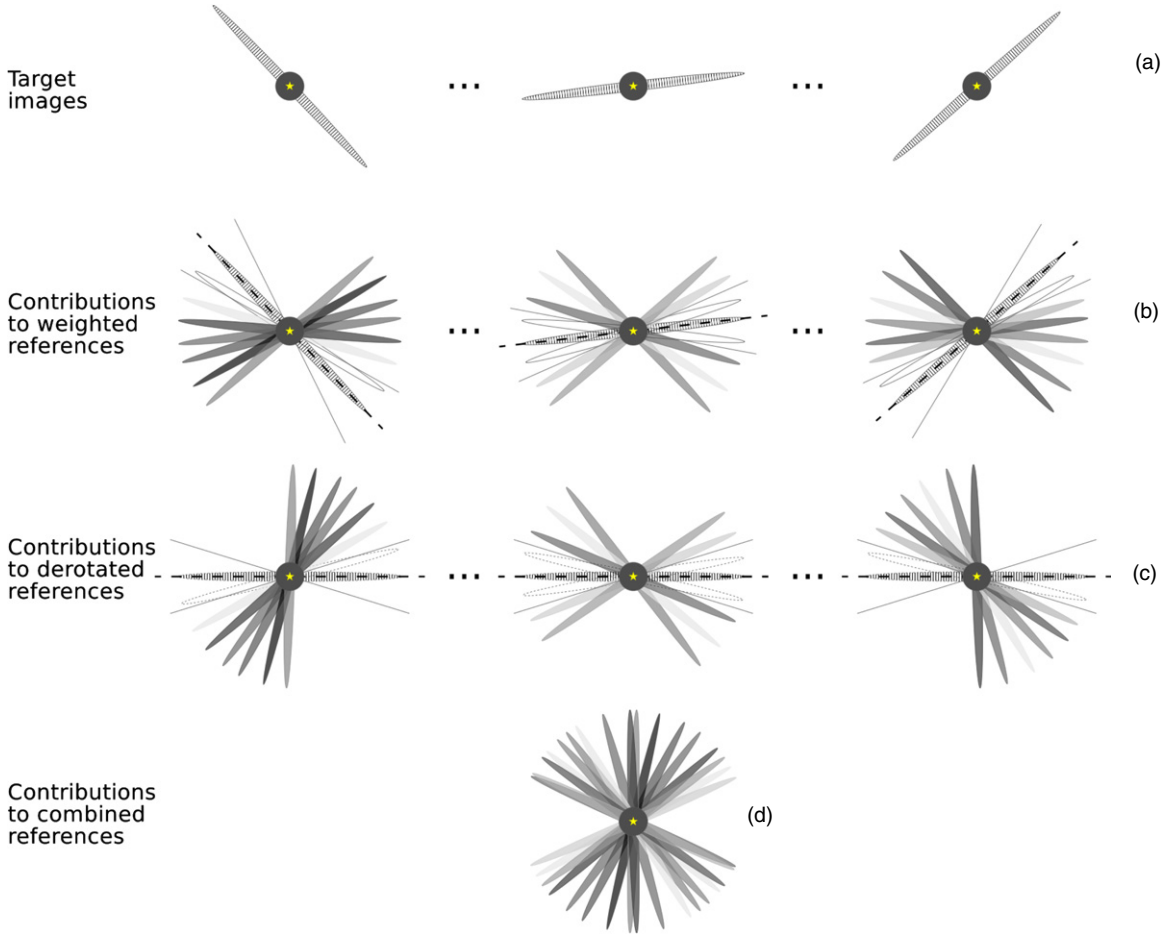

Figure 1. Illustration of the reference-image selection and combination process used in LOCI and our self-subtraction model. Ellipses represent edge-on disks arranged at various P.A.'s according to the parallactic rotation in a synthetic data set, while the dark gray circle is centered on the star and masks the region inside of a coronagraph's inner working angle. The gray level of an ellipse indicates the weight of that image in the reference PSF combination as determined by the $c_{ij}(r)$ coefficient (darker means more heavily weighted). In row (a), the disks of the target images $T_i(r, \theta)$ are positioned at their associated θ_i. In row (b), the disks of the reference images $T_j(r, \theta)$ are weighted by their c_{ij} and summed to create the reference PSF for T_i. The disk of the target image and disks located within the minimum rotation threshold for a given separation r (marked by solid lines and white fill) have $c_{ij}(r) = 0$ and do not contribute to the reference PSF. Note that the amount of P.A. rotation is exaggerated in this diagram for clarity, leading to fewer disks with $c_{ij}(r) = 0$ than in a typical real data set. In row (c), all reference PSFs from row (b) are derotated so that the midplane of the target image's disk lies at $\theta = 0^\circ$. In row (d), all reference PSFs from row (c) are aligned to the star and summed to create the self-subtraction function for the final LOCI-processed image at separation r.

(A color version of this figure is available in the online journal.)

annuli and not sectors within those annuli. It follows that the reference PSF-subtracted target image is

$$S_i(r, \theta) = T_i(r, \theta) - \sum_j c_{ij}(r) T_j(r, \theta). \quad (2)$$

We build the final image F by rotating all S_i to align with a common sky frame and then combining those rotated PSF-subtracted images. We use the mean here for simplicity of computation; other schemes are possible (e.g., median, weighted mean). The final image is

$$F(r, \phi) = \frac{1}{N} \sum_i S_i(r, \phi + \theta_i) \quad (3)$$

$$= \frac{1}{N} \sum_i \left[T_i(r, \phi + \theta_i) - \sum_j c_{ij}(r) T_j(r, \phi + \theta_j) \right] \quad (4)$$

$$= g(r, \phi) - \frac{1}{N} \sum_{i,j} c_{ij}(r) g(r, \phi + \theta_j - \theta_i). \quad (5)$$

We can express $g(r, \phi + \theta_j - \theta_i)$ as the convolution of $g(r, \phi)$ with a delta function located at $\theta = \phi - \Delta\theta_{ij}$, where $\Delta\theta_{ij} \equiv \theta_i - \theta_j$. Here one could incorporate blurring due to field rotation by replacing the delta function with a function of finite width, such as a top hat. Our final expression for the LOCI-subtracted field then becomes

$$F(r, \phi) = g(r, \phi) - g(r, \phi) \otimes \sum_{i,j} c_{ij}(r) \delta(\phi - \Delta\theta_{ij}). \quad (6)$$

The second term in Equation (6) represents the "self-subtraction function" z,

$$z(r, \phi) = g(r, \phi) \otimes \sum_{i,j} c_{ij}(r) \delta(\phi - \Delta\theta_{ij}). \quad (7)$$

The self-subtraction function is the linear combination of scenes weighted and positioned in the same manner as the images in the reference PSFs at a given radius. Thus, subtracting this function from the general scene g will cause self-subtraction in the final image F in the same locations and with the same amplitude as in the final LOCI-processed data.

An accurate calculation of the self-subtraction function is important to the quantitative investigation of structure in debris disks. LOCI parameters are tuned to maximize the signal-to-noise ratio (S/N) with respect to random errors, while the self-subtraction function attempts to quantify systematic errors. Efforts to infer disk structure from ADI data must consider both types of error.

Forward modeling has advantages over an alternative scheme to account for self-subtraction, namely, injecting a model disk at a different nonoverlapping angle and reducing the augmented data. This injection introduces random noise from the raw data into the self-subtraction function. Any comparison of a self-subtracted model with LOCI-processed data will then have two random noise contributions and, thus, two sources of uncertainty in the surface brightness. The speckle pattern near the synthetic disk may also differ from the pattern near the real disk, complicating comparison of the two after reduction. In contrast, the forward-modeling method produces a self-subtraction function free from random noise, so that the random error in a comparison of model with data comes only from the data. In practice, it may also be difficult to find a position in the data at which to inject the model disk, because of interference from diffraction spikes or artifacts caused by telescope support struts. This is not an issue when using the forward-modeling technique, because no alterations are made to the data itself.

Another key advantage of our technique is that it only requires a single LOCI reduction of the data set (or one reduction per N_δ-value if multiple N_δ's are used, as discussed in Section 3.4). This means less computational expense and greater speed than methods that require LOCI reductions of multiple model-injected data sets. This speed advantage persists when comparing our technique with another method for correction of self-subtraction that subtracts a model disk from the unreduced data and then measures the residuals after reduction, which was used by Thalmann et al. (2013) in conjunction with PCA forward modeling to determine self-subtraction of disk emission, thereby avoiding introduction of additional noise sources associated with model injection. Such efforts present an interesting future avenue of investigation in comparing our LOCI-based technique with PCA-based methods, but we consider it to be outside the scope of this work.

Finally, we suggest that it should be straightforward to adapt the self-subtraction modeling algorithm to schemes involving linear combinations of images in ADI sequences other than the LOCI version we employ in this work. For example, the algorithm can be adapted to different image-weighting schemes and has no restrictions on the number of images in the data set. This may prove useful as new ADI-related methods are developed for the coming generation of instruments operating behind extreme-AO systems that aim to reach higher contrasts and smaller inner working angles than current instruments (e.g., GPI, SPHERE, SCExAO; Macintosh et al. 2008; Beuzit et al. 2008; Guyon et al. 2011).

3. MODEL APPLICATION TO HD 32297

We applied the general self-subtraction modeling process outlined in the previous section to the specific case of the HD 32297 debris disk. This allowed us to test the effectiveness of the modeling method and also to derive brightness profiles for the disk that were unbiased by self-subtraction. HD 32297 was also chosen in part to investigate disagreements between brightness measurements from prior ground- and space-based observations. Brightness profiles that reflect the true dust distribution are necessary if we are going to use them to infer physical properties of the disk. In addition, accurate characterization of self-subtraction in our LOCI-processed images will be critical to future comparisons of observations with models of the disk surface brightness.

Previous observations of the HD 32297 debris disk have covered a wide range of wavelengths. Schneider et al. (2005) revealed a disk extending from ∼34 to 400 AU in radius at 1.1 μm using NICMOS aboard *HST*. They modeled the disk to be $10\overset{\circ}{.}5 \pm 2\overset{\circ}{.}5$ from edge-on and reported a brightness asymmetry in which the southwest (SW) ansa was brighter than the northeast (NE) ansa. Kalas (2005) made ground-based, seeing-limited *R*-band observations from Mauna Kea that detected scattered light at larger scales (580–1680 AU) and found a brightness asymmetry similar to that of Schneider et al. (2005). Kalas (2005) also reported P.A.'s of the emission midplanes to the NE and SW that diverged by 31°. To explain these asymmetries, the authors proposed a collision of the disk with a clump of interstellar material as HD 32297 moves southward through the interstellar medium (ISM).

At mid-infrared wavelengths, Moerchen et al. (2007) observed the NE lobe to be brighter than the SW at 12 μm beyond a radius of $0\overset{''}{.}75$ with T-ReCS at Gemini South but saw no significant asymmetry at 18 μm. This work and Fitzgerald et al. (2007; 11 μm imaging with the Michelle spectrograph at Gemini North) suggest that there is a ring of warm, submicron-sized dust grains that becomes depleted within a radius of ∼70 AU. Resolved 1.3 mm imaging from the Combined Array for Research in Millimeter-Wave Astronomy conducted by Maness et al. (2008) showed the same SW–NE asymmetry as the near-infrared and optical studies. Such a disparity in the degree of asymmetry among different wavelengths is predicted by some planet-induced resonance models (Wyatt 2006), encouraging further study of this system. In the far-infrared, Donaldson et al. (2013) combined *Herschel* photometry with previous measurements to investigate the spectral energy distribution (SED) of the disk. Their best-fit SED model indicated a cold outer dust ring centered around 110 AU and a warm inner disk with an inner radius of ∼1.1 AU.

Debes et al. (2009) imaged the HD 32297 debris disk at 1.6 and 2.05 μm with NICMOS and also reexamined the archival 1.1 μm data collected by Schneider et al. (2005), all of which indicated the previous SW–NE asymmetry. In addition, they reported warping of the inner disk (<400 AU), which they modeled as the result of an interstellar cloud sculpting the disk material (similarly to Kalas 2005). Using the Palomar AO system's deformable mirror mapped to a 1.6 m subaperture of the Hale Telescope, Mawet et al. (2009) detected a truncation of the NE ansa at ∼65 AU as well as a clear SW–NE asymmetry in K_s-band imaging, in accordance with previous studies. Recently, Boccaletti et al. (2012) presented Very Large Telescope NACO AO imaging processed with various versions of ADI in *H* and K_s that did not show any significant asymmetry but did show the NE ansa to be elongated relative to the SW. They also found midplane curvature between ∼65 and ∼110 AU (more significantly on the NE ansa than the SW). Currie et al. (2012b) reduced Keck NIRC2 K_s data using a "conservative" LOCI algorithm and detected a SW > NE asymmetry at small separations (∼55–65 AU), but their radial brightness profiles also exhibited an unmentioned NE > SW asymmetry at $r \approx$ 120–145 AU. They reported a northward disk curvature similar to those found in the previously mentioned works, as well. The circumstellar environment of HD 32297 is also unique because

of a significant gas component detected in Na I absorption by Redfield (2007) and in [C II] emission by Donaldson et al. (2013), a rarity for debris-disk systems.

3.1. Observations

We observed HD 32297 using the Keck II AO system and a coronagraphic imaging mode of the NIRC2 instrument. We took 30 images with individual exposure times of 30 s in the *H*-band filter ($\lambda_0 = 1.63\,\mu$m, $\Delta\lambda = 0.296\,\mu$m) on 2005 October 22 and nine images with individual exposure times of 60 s in the K_s filter ($\lambda_0 = 2.15\,\mu$m, $\Delta\lambda = 0.311\,\mu$m) on 2007 September 22. The camera was operated in "narrow" mode, with a $10'' \times 10''$ FOV and a pixel scale of 9.95 mas pixel^{-1} (Yelda et al. 2010). A coronagraph mask of 200 mas radius artificially eclipsed the star in the *H* science images, while a 400 mas mask was in place for K_s science images. Air mass ranged from 1.02 to 1.20 across the two nights, and the AO loop was closed with HD 32297 serving as its own natural guide star. The PSF FWHM was within 10% of the diffraction limit in all images, with the diffraction limit at the central wavelength equal to 41 mas (4.1 pixels) in *H* and 54 mas (5.4 pixels) in K_s.

We employed ADI for all science observations. Using this technique, we acquired a sequence of images with the camera rotator in vertical-angle mode, in which the altitude–azimuth mounted telescope and the rotator were adjusted such that the telescope PSF's orientation was held fixed relative to the camera and AO system optics. This caused the FOV to rotate throughout the sequence while the PSF orientation was fixed relative to the detector. Our images spanned $30\overset{\circ}{.}5$ of angular rotation in the *H* data set and $37\overset{\circ}{.}2$ in K_s.

For calibration purposes, we observed standard stars SJ 9105 (Persson et al. 1998) and FS 30 (Hawarden et al. 2001) unocculted to determine the photometric zero point in *H* and K_s bands, respectively. We note that our observations of SJ 9105 showed it to be a visual double, with a second source $\sim 0\overset{''}{.}5$ to the southeast of the standard star. Although the second object is relatively faint (total flux only $\sim$4% that of the standard), it may have affected our calculation of the photometric zero point and systematically biased our photometry downward by $\sim$4%. Flux densities used for flux conversion were taken from Tokunaga & Vacca (2005).

3.2. Data Reduction

We used the same procedure to reduce both the *H* and K_s data sets. After bias subtraction and flat-fielding, we masked cosmic-ray hits and other bad pixels. Next, we aligned the individual exposures by cross-correlation of their stellar diffraction spikes (Marois et al. 2006). Following this, radial profile subtraction suppressed the stellar halo and the sky background by effectively acting as a high-pass filter.

We applied a modified LOCI algorithm (Lafrenière et al. 2007) to our data to suppress the stellar PSF and quasi-static speckle noise. For each image in a data set, LOCI constructs a unique reference PSF from an optimized linear combination of other images in the data set. The reference is constructed in azimuthally divided subsections of annuli centered on the star. In each subsection, the coefficients c_{ij} of the linear combination are chosen so as to minimize the residuals of the PSF subtraction. To simplify our self-subtraction modeling procedure (see Section 3.4 for further explanation), we modified the LOCI algorithm to first compute the coefficients as functions of both azimuthal angle and radius, following the prescription presented by Lafrenière et al. (2007). Then the algorithm takes the median of each c_{ij} across all subsections in a given annulus and replaces the original coefficient with that median value. Only after this do we perform the linear combination that creates the reference PSF subsection. This reduces c_{ij} to being only a function of radius and provides a single coefficient per annulus for each image, as described in Section 2.

After using LOCI to subtract the stellar PSF from all images in the data set, we derotated the PSF-subtracted images and then averaged them to create our final image. Averaging, rather than median combination, was important for preserving the linearity necessary for self-subtraction modeling and for simplifying the calculation of the self-subtraction function (see Section 2).

We maximized the S/N of the final image by tuning the LOCI parameters to achieve a balance between noise attenuation and disk flux retention. The S/N used in tuning LOCI parameters was calculated by performing aperture photometry at multiple, equally spaced radial separations between $r = 21$ and $r = 300$ pixels. We tuned five LOCI parameters. The azimuthal width of the disk PSF is given by W (in pixels), and N_δ represents the minimum gap allowed (in units of W) between the disk midplane in the target image and the midplanes in the images used as references. The radial width of the subtraction subsections, in which the subtraction residuals are locally minimized, is set by dr (in pixels). The parameters g and N_a are dimensionless and, along with W, determine the radial and azimuthal widths of the optimization subsections. See Section 4.1 of Lafrenière et al. (2007) for more detailed definitions of all five parameters.

For the *H*-band data, we determined optimal parameter values of $W = 10$ pixels ($\sim$11 AU), $N_\delta = 0.5$, $dr = 5$ pixels ($\sim$5.5 AU), $g = 0.1$, and $N_a = 250$. Our value for W is based on an estimate of the average disk FWHM at small r. For the K_s data, we determined slightly different optimal values of $W = 10$ pixels, $N_\delta = 0.25$, $dr = 5$ pixels, $g = 0.1$, and $N_a = 150$. Additional images were created from each data set for use in our profile-fitting routine (Section 3.4), with values of N_δ ranging from 0 to 5 and the other parameters set to their optimal values above.

3.3. PSF-subtracted Images

We present the final LOCI-processed *H*- and K_s-band images in Figure 2. We spatially resolved the disk in scattered light at projected separations of $\sim$50–300 AU ($0\overset{''}{.}45$–$2\overset{''}{.}7$). Residual speckle noise significantly contaminates the disk emission inward of 50 AU and creates confusion with the disk signal. Negative-brightness regions occur above and below the disk midplane as a result of self-subtraction by LOCI processing.

Upon visual inspection, the ansae appear largely symmetric in brightness and size in both bands. The only apparent feature is a curvature of both ansae toward the northwest that is more pronounced at larger separations. This curvature is discussed in more detail in Sections 3.5.4 and 4.4.

3.4. Brightness Modeling Accounting for Self-subtraction

To demonstrate the effectiveness of our self-subtraction modeling algorithm, we applied it to our observations of the HD 32297 disk. By combining the framework from the previous sections with a simple parameterization of the disk's brightness distribution, we produce a model of the two-dimensional surface brightness as it appeared before undergoing LOCI self-subtraction. We then extract radial profiles for disk parameters, such as the one-dimensional integrated brightness, from this

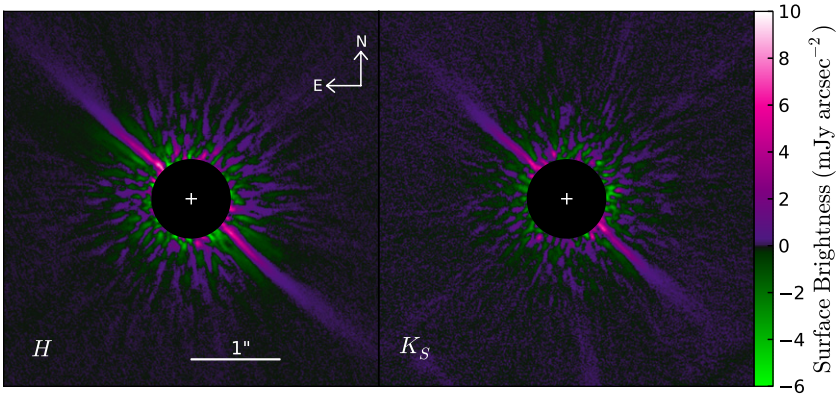

Figure 2. Final LOCI-processed images of the disk surface brightness in scattered light in H (left) and K_s (right) bands. The disk is seen approximately edge-on with one ansa to the NE and the other to the SW of the star. Green areas are negative-brightness regions created by self-subtraction or imperfect PSF subtraction. The star's location is marked by a white cross. The black circle masks the innermost radii, where either residual speckle noise dominates or the coronagraph mask obscures the disk.

(A color version of this figure is available in the online journal.)

model to investigate the distribution of dust in the disk. This method is slightly more complex than aperture photometry, but it produces brightness measurements that are largely independent of the self-subtraction. It also avoids complicated three-dimensional radiative transfer models and data inversion. Our goal is not necessarily to produce a perfect representation of the disk but rather to construct a model that is useful for verification of our self-subtraction modeling method and for estimating the disk's physical parameters. These estimates can later be used as starting points for constructing more complex three-dimensional models that may provide more accurate measurements of those parameters.

We begin by defining two coordinate systems so that we can more easily extract data from our images and also construct models to compare with those data. The first is a standard Cartesian coordinate system (x, y) with the star at the origin, x along the horizontal axis (positive to the right), and y along the vertical axis (positive up). The second is a polar coordinate system (r, θ) with the star at the origin and $\theta = 0^\circ$ along the positive x-axis. We then rotate the final LOCI-processed image counterclockwise by 42.°5 (the complement of our estimated disk P.A. of ∼47.°5), so that the disk midplane lies roughly along the x-axis, and divide the image in two along a line parallel to the y-axis and passing through the star location. This gives us separate SW and NE sections of the image and allows us to deal with one ansa at a time.

For one of the ansae, we further divide the corresponding image section into semicircular annuli (semiannuli) that are centered on the star, have the center of their arc aligned with $\theta = 0^\circ$, and are 1 pixel wide in the radial direction. Each semiannulus contains the disk's one-dimensional brightness profile at $r = r_0$, where r_0 is equal to the semiannulus's radius of curvature. For computation purposes, we project the semiannulus onto a line, changing coordinates of the semiannuli from polar to Cartesian via the transformations $y = r \sin\theta$ and $x = r$. This makes the brightness profiles functions of vertical (y) and radial (x) distance from the star. These one-dimensional vertical profiles represent the data to which we fit our self-subtraction model. Figure 3 shows example profiles from our H-band data set processed with various N_δ-values (with y plotted along the horizontal axis).

Next, our model function for the scene g (as defined in Section 2) represents an estimate of the disk vertical brightness

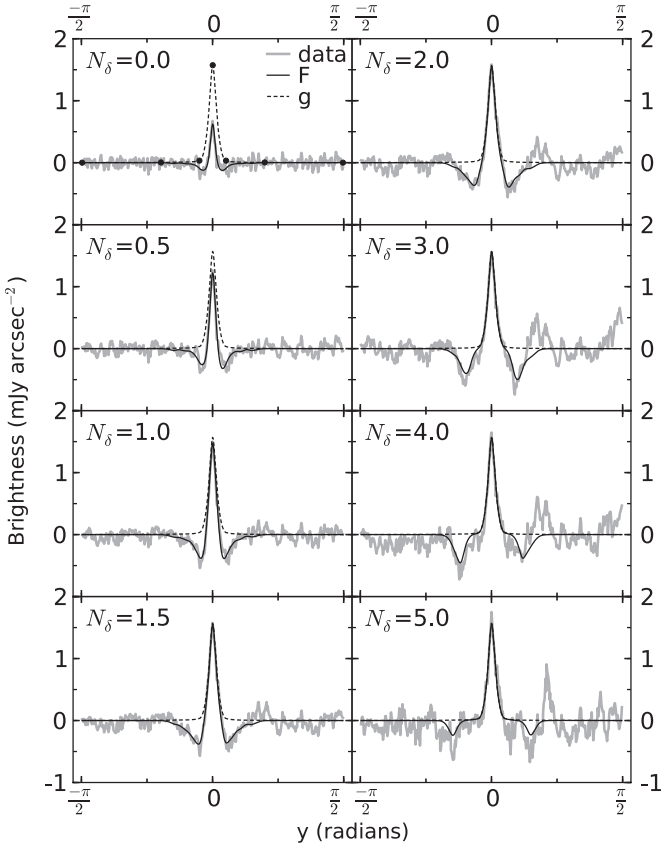

Figure 3. Examples of one-dimensional semiannuli fitted by our self-subtraction modeling algorithm. The different panels show semiannuli from the H-band images reduced using different N_δ-values, but all from the SW ansa at $r = 133$ AU. The thick gray lines represent the data, the solid black line is the self-subtracted model (F) fit to the data, and the dashed line is the best-fit cubic spline model of the underlying disk vertical brightness profile (g), with filled circles marking the control-point locations in the first panel. The scene g is constant in all panels, but the self-subtracted model differs according to N_δ.

profile before it underwent self-subtraction. In this case, we approximate the shape of the disk's vertical profile using a monotonic cubic spline. For simplicity, we assume the profile is symmetric about the disk midplane and that the peak brightness occurs at the midplane. We divide the profile at the midplane and select four interpolation control points along one half of the

profile. One control point is located at the peak, one is located in the wing of the profile, another is in the profile tail, and the final point is positioned at the end of the tail. The brightnesses of these control points are variables, b_0, b_1, b_2, and b_3, respectively. Both b_0 and b_1 are allowed to vary in the least-squares fit. We fix $b_2 \approx b_3 \approx 0$, assuming that the disk flux is negligible far from the midplane. This number of control points sufficiently approximates the general shape of the disk's vertical profile for our proof-of-concept test without compromising computational speed. Adding more control points would likely be one way to improve upon our model and increase the accuracy of our measurements. Once values for the control points are assigned, we reflect them about the midplane so that we can interpolate the entire profile. We do so over the range y to obtain g, which we insert into a one-dimensional version of Equation (6) that replaces r and θ with x and y. The third and final fit parameter is the position of the midplane ($y_{\rm mid}$), which sets the position of the peak control point along y.

We derive initial estimates for the fit parameters from a Lorentzian profile assumed to have a peak brightness equal to the maximum brightness of the vertical profile and a FWHM drawn from a power law established from a conservative (large N_δ) reduction of the data. The three parameters depend only on x, and therefore the function g that they produce is also a function of x. Early tests showed that a pure Lorentzian function does not approximate the shape of the disk well at all separations, leading us to use the spline as our model function. We chose a simple model for the vertical profile because our primary objective was to verify our procedures for modeling self-subtraction in the disk and not necessarily to model the disk itself in fine detail.

As Figure 1 (row (a)) illustrates, the disk is oriented at a different P.A. in each image in the data set. Data recorded at the telescope during observations provide the P.A.'s for each image (θ_i), which we transform to y_i and insert into the self-subtraction function (Equation (7)). The same coefficients c_{ij} used in the LOCI processing of the image being modeled are also substituted into the expression. We include an additional weighting coefficient in the summation in Equation (7) based on a rough approximation of the Strehl ratio[3] of each reference image T_j. This weighting attempts to account for variations between images due to seeing, and it is only applied during modeling. The Strehl ratio was fairly stable and the PSF core remained diffraction-limited across the observations, as weights for both data sets were in the range 0.9–1.2 (with 1.0 as the mean). As shown in Figure 1 (row (b)), for a given target image T_i, some T_j have $c_{ij} = 0$ because those reference images are excluded from the reference PSF based on insufficient field rotation (the minimum threshold being set by LOCI parameters $N_\delta \times W$). With all of the components assembled, we compute the self-subtraction function in Equation (7) and then insert this into Equation (6) to produce a self-subtracted model of the vertical profile, which we call F.

We use a weighted least-squares routine to compare F with the observed profile and determine the best-fit values for b_0, b_1, and $y_{\rm mid}$. Each pixel i in the observed profile is weighted by an estimated measurement uncertainty σ_i. We calculate this uncertainty as $\sigma_i = \sqrt{\sigma_{{\rm phot},i}^2 + \sigma_{\rm back}^2}$, where $\sigma_{{\rm phot},i}$ is the photon noise at that pixel and $\sigma_{\rm back}$ is the background noise at the radial location of the profile due to residual speckles and sky background. The photon noise cannot simply be measured from the observed profile, because LOCI self-subtraction has created "negative-brightness regions" that distort the photon counts. Instead, we estimate the photon noise as the square root of the pixel's photon count in the model scene g constructed for each least-squares iteration and propagate this uncertainty through the modeling algorithm. This is only a rough estimate that attempts to account for the photon noise per pixel before it was distorted by self-subtraction. The background noise is calculated as the standard deviation of the pixel brightness in the regions of the observed profile that contain neither disk signal nor self-subtraction.

We performed the least-squares fit simultaneously on profiles from LOCI-processed images of varying N_δ at each separation, which means that a separate model F is constructed for each N_δ. For our H-band data, we use eight images with $N_\delta = \{0, 0.5, 1, 1.5, 2, 3, 4, 5\}$, where $N_\delta = 0$ is the most aggressive reduction (all reference images allowed) and $N_\delta = 5$ is the most conservative (few reference images allowed). For our K_s data, we use nine images with $N_\delta = \{0, 0.25, 0.5, 1, 1.5, 2, 3, 4, 5\}$, with the $N_\delta = 0.25$ image included because it showed the highest overall S/N for this data set. All images are weighted equally. This inclusion of data processed with multiple N_δ-values helps the algorithm select a model scene g that accurately fits the data over a wide range of self-subtraction levels. The parameter space of the fit is restricted in two ways. We require that (1) the midplane position be within the range y of a given profile and (2) $b_1 \geqslant b_2$, to maintain consistency within the monotonic cubic spline interpolator. The least-squares algorithm produces a covariance matrix Σ for the parameters b_0, b_1, and $y_{\rm mid}$.

Examples of the best-fit models F and g for a simultaneous fit to vertical profiles at the same separation but from different-N_δ reductions of the H-band data are shown in Figure 3. The underlying scene g is constant for all panels, but the self-subtraction function differs for each N_δ, resulting in different functions F.

The best-fit model function g is used to derive the disk brightness and FWHM. We calculate a one-dimensional integrated brightness (Graham et al. 2007) by integrating g over all y. We calculate the disk FWHM directly from g in a straightforward fashion. These parameters are more relevant to the disk's physical properties than the fit parameters b_0 and b_1. The midplane position is taken directly from the least-squares fit as the best-fit value for $y_{\rm mid}$.

It is important to note that because the vertical profile model takes self-subtraction into account, the best-fit values retrieved for the brightness, projected FWHM, and midplane location are those of the model disk *prior to self-subtraction*. Assuming that the model is an accurate description of the disk, we then gain estimates of the true disk parameters, uncorrupted by LOCI processing. The procedure described in this section for HD 32297 only models the disk at a single radius, so we repeat it for all radii and for both ansae to construct the full two-dimensional brightness distribution, in the process obtaining radial profiles for one-dimensional integrated brightness, projected FWHM, and midplane position.

3.4.1. Uncertainties in Brightness Modeling

We determine the uncertainties on our derived disk parameters from transformations of the covariance matrices (Σ) associated with the original parameters from the least-squares fits. Correlations exist between the derived parameters, and to transform the variables along with their uncertainties, we must account

[3] As a proxy for the Strehl ratio, we used a circular aperture of radius 3 pixels to measure the flux of the star through the coronagraph mask in an image relative to the mean of this flux across all images in the data set.

for the Jacobian of the transformation. To do this, we calculate $\Sigma' = J \cdot \Sigma \cdot J^T$, where Σ' is the transformed covariance matrix for the derived parameters and J is the Jacobian, which we compute numerically. Finally, taking the square root of the variances along the diagonal of Σ' gives the marginal distribution σ for all three derived parameters. These uncertainties include contributions from both photon noise and background noise, because those terms compose the least-squares weights.

Estimating parameter uncertainties from the least-squares covariance matrices assumes independent, Gaussian-distributed measurement uncertainties. For simplicity in this proof-of-concept application, we will work under this assumption, although we recognize that speckles are not Gaussian-distributed (e.g., Fitzgerald & Graham 2006) and that spatial correlations exist between image pixels. We explore the effects of the non-Gaussian speckle distribution on our uncertainty estimates near the end of this section. Despite these issues, we generally find that derived-parameter measurements in adjacent separation bins agree within their 1 σ errors (Section 3.5). This suggests that our errors properly represent pixel-to-pixel variations in the data, even in the low-S/N regions of the disk.

However, we note the important caveat that there may be systematic errors for which our 1 σ uncertainties do not fully account. One possible source of such systematic error would be an inability of our spline model for the disk vertical profile to match the functional form of the profile. Such a situation could lead the least-squares fit parameters to be overconstrained, consequently causing variances in Σ (and therefore in Σ') to underestimate the true parameter variances. This should be taken into account when evaluating the significance of features in the radial profiles of Section 3.5. Violation of our assumption that the disk brightness is symmetric around the midplane is another potential source of systematic error. An improved model of the disk vertical profile could reduce these errors, which remain preferable to the relatively large uncertainties introduced by self-subtraction and removed by our modeling process.

One way we attempt to mitigate underestimation of systematic errors is by scaling the covariance matrix by the reduced chi-squared value (χ^2_ν). With mean χ^2_ν-values of $\sim$4.8 for K_s model fits and $\sim$6.0 for H model fits, this scaling increases the associated σ-errors on our derived disk parameters by factors of $\sim$2.2–2.4 on average. In calculating χ^2_ν, we exclude the residuals from pixels that do not contain either disk signal or self-subtraction. These pixels contain only random noise and are best fitted by zero brightness in the model profile. Such "empty" pixels make up a significant fraction of each profile and may bias the χ^2_ν downward if not excluded, thereby implying a better goodness of fit than is deserved. The disk and self-subtraction signals are spatially correlated as a consequence of the diffraction-limited imaging resolution, so we determine the number of degrees of freedom (ν) as the number of resolution elements minus the number of fit parameters. The number of resolution elements is approximated as the number of pixels in the profile divided by the diffraction limit (in pixels). This is a more accurate estimate of the degrees of freedom because our model will only be sensitive to features larger than the diffraction limit.

The χ^2_ν metric is itself uncertain, so we must consider how our scaling of the parameter variances by χ^2_ν introduces additional uncertainty. The standard deviation for a chi-squared distribution is proportional to $\frac{\sqrt{2}}{\nu}$. Conservatively assuming that the quasi-static speckles follow an exponential distribution, we find that we need $\nu \gtrsim 200$ for a given semiannulus in order to achieve a fractional uncertainty on χ^2_ν of $\lesssim$20%. Semiannuli only contain this number of degrees of freedom at $r > 290$ AU. Consequently, there is uncertainty in the scaling of our errors, particularly at small separations, where speckle noise is prominent. We do not include this additional uncertainty in our error bars, but it should be considered when evaluating the significance of our measurements.

We reiterate that our goal in this work is not to produce a perfect representation of the disk but rather to construct a model that is useful for verification of our self-subtraction modeling method and for estimating the disk's physical parameters. The estimates can later be used as starting points for constructing more complex three-dimensional models that may provide more accurate measurements of those parameters.

3.5. Modeling Results

We present the model surface brightness distributions produced by the process outlined in the previous section for the H and K_s bands in Figures 4 and 5, respectively. For display purposes, panels (a), (b), and (c) have been scaled by σ_i, which is the separation-dependent random error in the data at each pixel i, as calculated in Section 3.4. Note that this differs from the σ described in Section 3.4.1. Panel (a) in each figure shows the LOCI image from Figure 2 with a different color stretch and rotated counterclockwise by 42.°5 so that the midplane lies along the horizontal. In panel (b) is a model with self-subtraction included, constructed by solving Equation (6) for the best-fit parameter values at all radii. Negative-brightness regions created by self-subtraction are visible above and below the midplane in the model image, similar to the LOCI-processed data in location and amplitude. Panel (c) shows a model of the disk as it appeared before corruption by self-subtraction and random error, which is constructed from $g(r, \theta)$. The banded structures of the models are artifacts primarily due to fluctuations in the best-fit parameters of the one-dimensional models at neighboring separations. Panel (d) shows the same model as in (c) but with no scaling. Finally, panel (e) is a deviate map calculated as $((a) - (b))/\sigma_i$. The deviates were not scaled by χ^2_ν and thus do not account for correlated pixels or overconstrained model parameters. We note that the deviates are greater than $3\sigma_i$ in some parts of the disk, indicating imperfect agreement between data and model (see Section 4.1).

By inspection, the pre-self-subtraction models (panels (c)) are consistently brighter than the self-subtracted models (panels (b)) along the midplane and in the wings. This indicates that we have recovered disk brightness that was previously lost to self-subtraction. We use the pre-self-subtraction model to derive radial profiles for the disk brightness, projected FWHM, and midplane location.

3.5.1. Brightness Profiles

Figure 6 shows the radial brightness profiles produced by our modeling of the final LOCI-processed images in both bands. We plot the one-dimensional integrated brightness (mJy arcsec^{-1}), which is intrinsically absent of self-subtraction because the modeling process accounts for radius-dependent flux loss. The 1 σ errors on the measurements were derived from covariance matrices scaled by χ^2_ν, thereby accounting for some of the systematic errors related to our simplified disk model (see Section 3.4.1 for details). This applies to our FWHM, midplane location, and color measurement errors in the following sections as well.

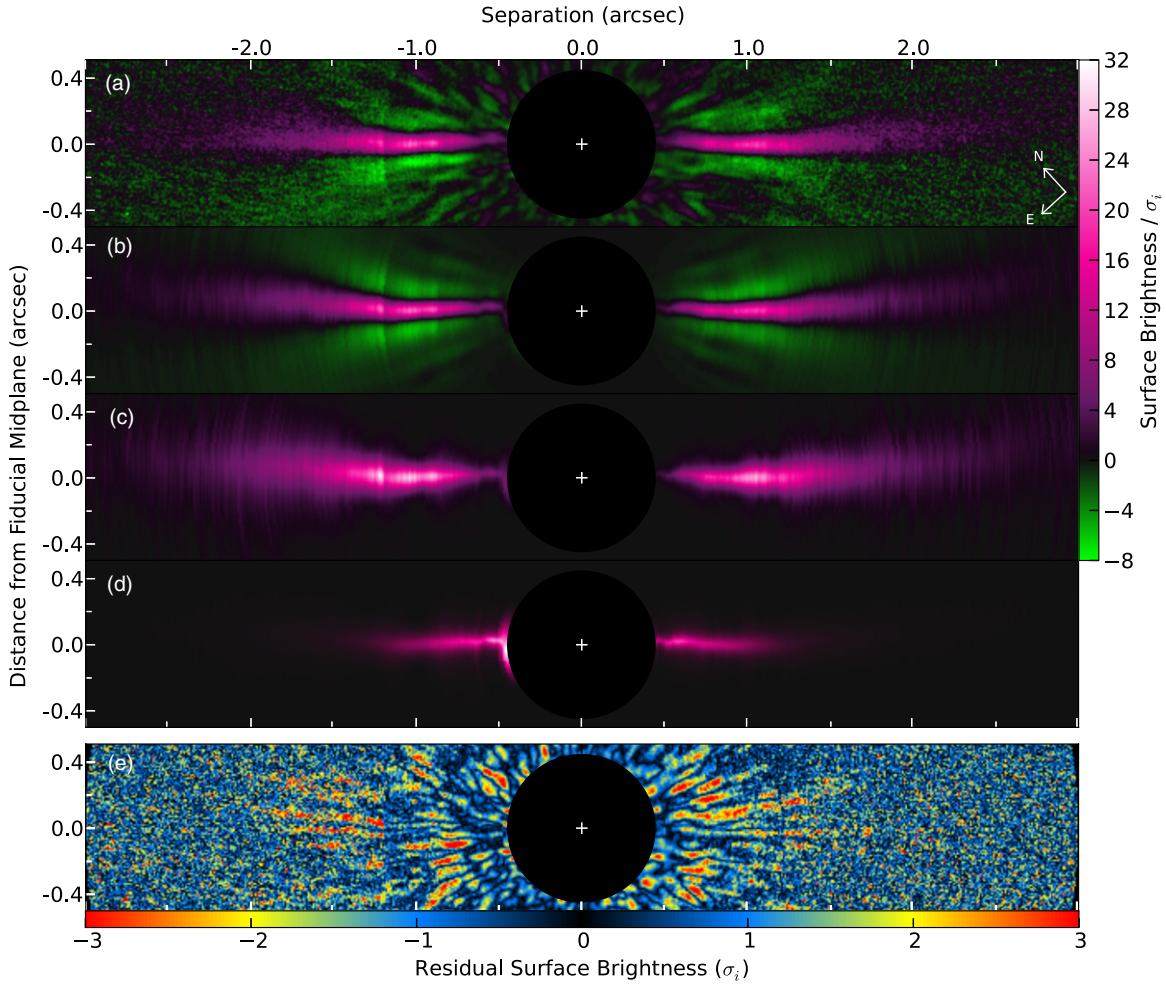

Figure 4. *H*-band images of the disk surface brightness. All panels except (d) have been scaled by σ_i, which is the separation-dependent random error in the data at each pixel i (not to be confused with σ calculated from a χ^2_ν-scaled covariance matrix). (a) LOCI-processed image from Figure 2, derotated by 42.°5 so that the fiducial midplane lies along the horizontal. (b) Model of the self-subtracted disk produced by subtracting the forward-modeled self-subtraction function from the best-fit model of the disk's underlying brightness distribution. Negative-brightness regions above and below the midplane match those in the real data. (c) Best-fit model of the disk's underlying brightness distribution absent of self-subtraction. Disk curvature toward the northwest is clearly visible. (d) Same as panel (c), except the brightness is not scaled by σ_i and follows a linear color stretch from 0 to 13 mJy arcsec^{-2}. (e) Deviate map for panels (a)–(c) normalized by σ_i. Note that the deviates were not scaled by χ^2_ν and thus do not account for correlated pixels or overconstrained model parameters.

(A color version of this figure is available in the online journal.)

The profiles extend inward to a separation of 50 AU (0.″45) in both bands. Interior to this point, the disk signal is dominated by residuals from incomplete PSF subtraction, and uncertainties on the brightness in this region are large. The profiles continue out to ∼335 AU (3.″0) in *H* and ∼160 AU (1.″4) in K_s. Beyond these separations, the disk brightness decreases to the level of the background noise and the disk is not detected. The S/N of the K_s data is lower than that of the *H* data at $r \gtrsim 160$ AU, leading to lower confidence in the K_s profiles at these larger separations.

We see brightness features in both ansae, but as is inherent in all high-contrast disk imaging, comparison with multiple independent data sources is necessary, because each telescope, instrument, observational technique, and data reduction method has its own distinct systematic errors. There is an additional complication in that different groups use different techniques for measuring brightness (e.g., flux in apertures of varying size, or midplane brightness). We note that all of the previous works discussed below used apertures of various sizes to extract surface brightness profiles, so our profiles are analogous but not directly relatable to theirs in an absolute sense (see Section 4.3 for further discussion).

The *H*-band brightness features are summarized here according to separation.

1. $r \lesssim 55$ AU. We measure an abrupt rise in NE brightness toward smaller radii. This could be due to contamination by speckle noise that is not adequately captured by our error bars (see Section 3.4.1 for details), or it could be similar to the steep increases reported by Schneider et al. (2005) and Currie et al. (2012b) at 1.1 μm and in K_s, respectively. However, we find the NE to be brighter than the SW in this region, which is opposite the asymmetry noted by the other two works.
2. $r \approx 90$, 130, 160–230 AU. We find a NE > SW asymmetry at these locations. The asymmetry at 130 AU coincides with a LOCI artifact on the NE ansa (possibly caused by a sharp transition between adjacent subtraction subsections with different noise characteristics) and may be an artificially produced increase in the NE brightness. Boccaletti et al. (2012) presented *H*-band profiles that showed no

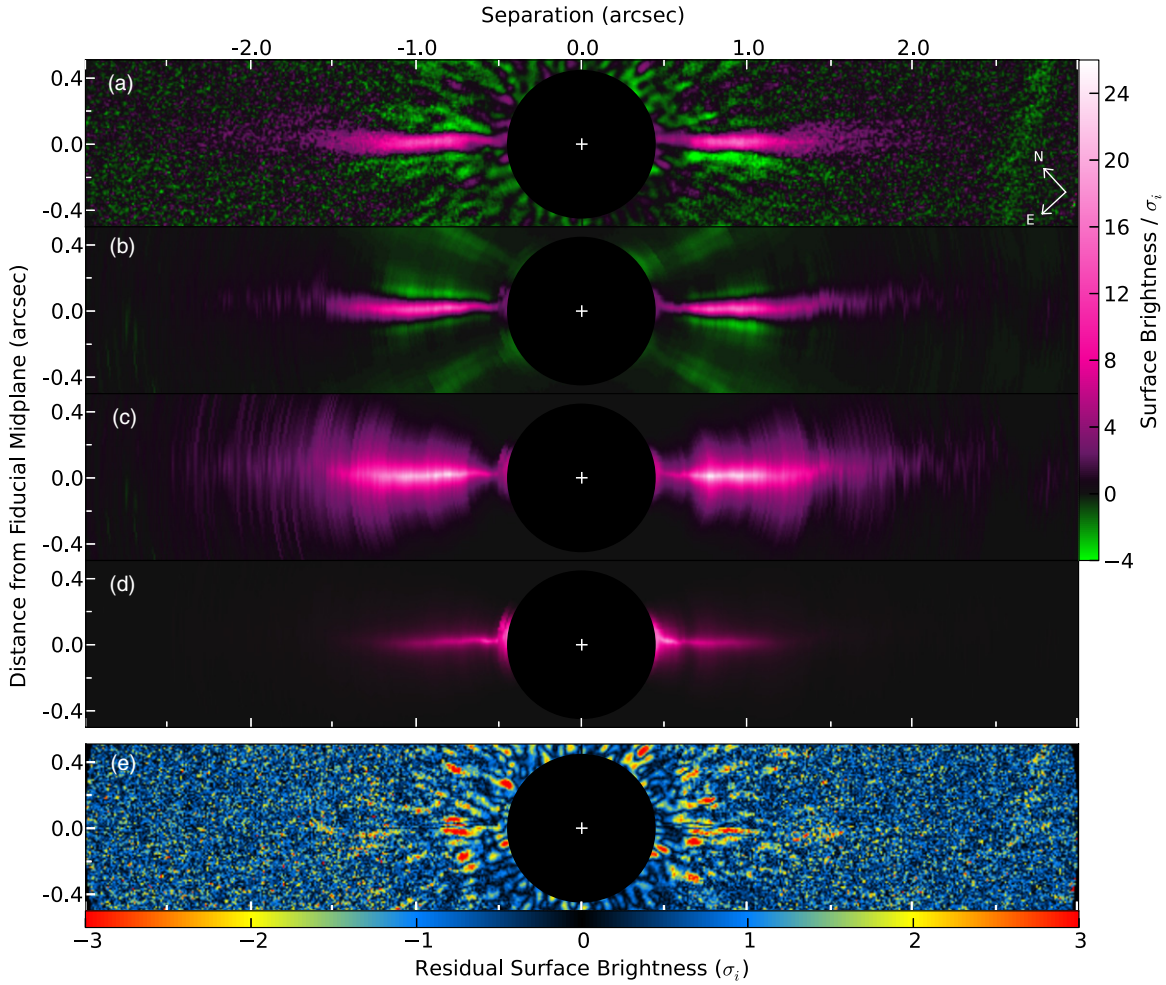

Figure 5. K_s images of the disk surface brightness directly analogous to the H images in Figure 4. The brightness scale for panel (d) is the same as in H, but the scale for panels (a)–(c) is slightly different than in H to better show the disk features.

(A color version of this figure is available in the online journal.)

statistically significant asymmetries. They processed their ground-based data with a "classical ADI" that they considered less aggressive than LOCI to try to preserve photometric fidelity. Our findings differ from the asymmetry detected at 1.6 μm by Debes et al. (2009), who noted the SW ansa to be significantly brighter than the NE ansa at $r \approx 112$–280 AU. Other space-based measurements by Schneider et al. (2005) at the shorter wavelength of 1.1 μm showed no statistically significant asymmetries between 56 and 190 AU, but those authors did report the SW ansa to be systematically brighter than the NE at $r \approx 157$–235 AU.

In K_s, we find the ansae to be generally symmetric, which agrees with Boccaletti et al. (2012), who presented ground-based K_s profiles that were symmetric between 56 and 336 AU. However, we do find asymmetries at these locations.

1. $r \approx 60$, 87 AU. We see SW > NE asymmetries at these separations, although the former feature is located at the edge of the speckle-dominated region.
2. $r \approx 115$ AU. We see a marginally significant NE > SW asymmetry here.
3. $r \approx 135$–180 AU. We note a NE > SW asymmetry in this low-confidence region. Partially overlapping this separation at $r \approx 120$–145 AU, profiles from Currie et al. (2012b) indicated a marginally significant NE > SW asymmetry in K_s, which was not remarked on. In contrast, Debes et al. (2009) noted a significant SW > NE asymmetry at 2.05 μm in the region $r \approx 112$–280 AU.

In addition, although we consider the $r > 275$ AU region insignificant for this band, we note that the dip in K_s SW brightness in this region is not a failure of the fitting algorithm but suppression of the disk in the LOCI image by an artifact present in several images of the data set.

On average, in the highest-confidence region, $r \approx$ 60–160 AU, the SW ansa is ~36% brighter in K_s than in H and the NE is ~23% brighter in K_s. This may be a real feature born of the disk's dust distribution, or as discussed in Sections 4.1 and 4.4.2, it could be due to extended wings in the model vertical profiles that increase the model FWHM and thereby increase the integrated brightness.

In general, we find the brightness profiles to be largely symmetric between ansae, but there are several regions of NE > SW asymmetry. Previous ground-based observations show similar asymmetries and elongation of the NE ansa (Currie et al. 2012b). These results differ from those of the NICMOS observations by Schneider et al. (2005) and Debes et al. (2009), which generally show the SW to be brighter than the NE. Such discrepancies between ground-based and space-based measurements underscore the different systematic uncertainties associated with both types of imaging. We have already discussed the

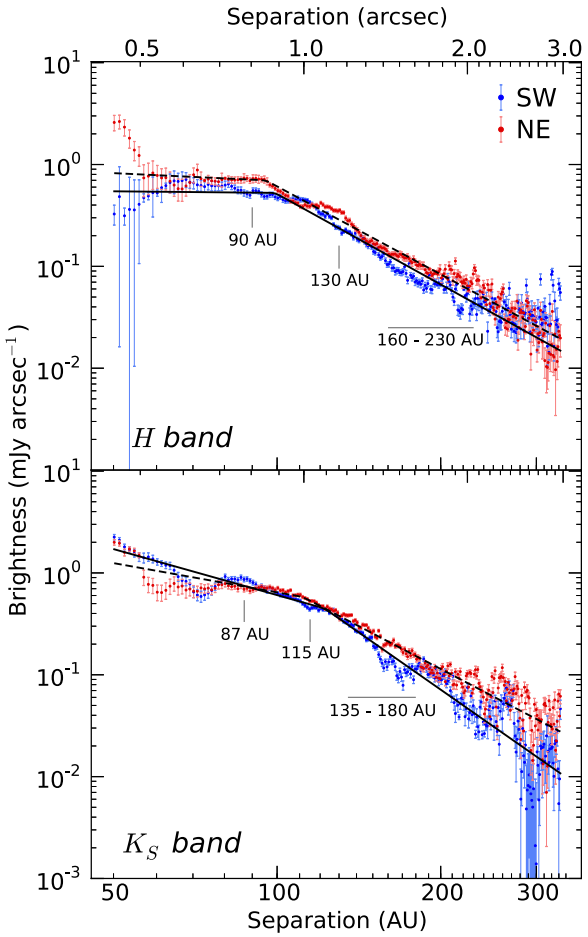

Figure 6. One-dimensional integrated brightness profiles produced by our self-subtraction modeling process in H and K_s. Measurements represent the disk brightness before flux loss caused by ADI/LOCI processing. The SW ansa is in blue and the NE is in red. Locations of significant asymmetries are labeled. The error bars represent 1 σ uncertainty levels that include χ^2_ν scaling and uncertainties associated with our simplified disk model, with the caveat that the errors may remain underestimated as a result of overconstrained least-squares fit parameters. The best-fit power-law functions are shown as solid lines for the SW and as dashed lines for the NE. Breaks in the power laws occur at $r \approx 95$–125 AU. Low S/N in the K_s data reduces the reliability of measurements at $r \gtrsim 160$ AU.

(A color version of this figure is available in the online journal.)

error sources associated with AO observations processed with ADI/LOCI. Although the NICMOS data do not suffer from ADI self-subtraction, they do not necessarily present unbiased photometry, because they could contain other image processing artifacts from a variety of sources (e.g., spectral mismatch between PSF reference star and HD 32297, telescope "breathing" (Fraquelli et al. 2004), unsubtracted thermal background, registration errors between stacked images). Systematic errors could impact the NICMOS photometry and therefore affect asymmetries in radial brightness profiles or disk colors (see Section 3.5.5).

3.5.2. Brightness Profile Power-law Fits

To characterize the change in brightness as a function of radius, we fitted broken power laws to each profile; the best-fit results are listed in Table 1. We fitted to the entire profile in each case. The relevant parameters are the location of the break ($r_{\rm break}$), power-law index interior to the break (α), and power-law index exterior to the break (β). The uncertainties shown

Table 1
Model Brightness Profile Power-law Best-fit Parameters

Band	Ansa	$r_{\rm break}$ (AU)	Inner Index (α)	Outer Index (β)
H	SW	99.1 ± 2.0	-0.05 ± 0.20	-2.95 ± 0.05
	NE	95.3 ± 2.1	-0.25 ± 0.28	-2.87 ± 0.03
K_s	SW	122.2 ± 1.9	-1.50 ± 0.07	-3.73 ± 0.07
	NE	111.4 ± 1.9	-0.95 ± 0.10	-2.79 ± 0.04

represent the 1 σ level. In H, the measurements of all three parameters are consistent between the two ansae. In K_s, $r_{\rm break}$ occurs ~10 AU farther out in the SW than in the NE. The indices α and β are also significantly steeper for the SW than the NE. In comparing the two ansae by wavelength, we find the SW and NE breaks to occur 10–20 AU farther from the star in K_s than in H. The K_s profiles also show steeper α-values and a steeper SW β-value than the H-band profiles.

We can compare our power-law results with those of previous works, again with the caveat that our profiles were derived in a different manner than the profiles in those works. Our H-band results for $r_{\rm break}$ are roughly consistent with those presented by Debes et al. (2009) for NICMOS 1.6 μm measurements, although our inner and outer indices are consistently shallower than theirs. Boccaletti et al. (2012) found $r_{\rm break}$ and β for their "classical ADI" H-band data that are approximately consistent with our own. Their α-values are positive and substantially different from ours, although they note that these measurements are uncertain as a result of low S/N in the inner regions of their H data. Perhaps because of differences in wavelength or instrument, our measurements differ from the shorter 1.1 μm results of Schneider et al. (2005). That work found a single power law in the SW, although the index (-3.57) was very similar to our outer index. They fitted a broken power law to the NE that had a greater $r_{\rm break}$ (190 AU) and a steeper inner index (-3.7) than ours but found a similar outer index (-2.74). At still shorter wavelengths, R-band profiles from Kalas (2005) yielded single-power-law indices of -3.1 ± 0.2 and -2.7 ± 0.2 for the SW and NE ansae, respectively, at $r \approx 5''$–$15''$, which, if extrapolated inward, would be similar to our outer indices.

With respect to the K_s-band results, our values for $r_{\rm break}$ roughly agree with the 2.1 μm values from Debes et al. (2009). Our SW β and NE α are also consistent with their findings, but our SW α is steeper by a factor of ~3 and our NE β is ~1.4 times shallower than theirs. The Boccaletti et al. (2012) K_s SW parameters are similar to the Debes et al. (2009) SW values, and thus our SW results compare similarly. In the NE, we record a similar $r_{\rm break}$ and α but a shallower β (by a factor of ~1.6) than reported by Boccaletti et al. (2012). Finally, Currie et al. (2012b) found they could not fit a power law to their K_s profiles inward of ~112 AU, which is roughly consistent with the location of our break. However, they found much steeper power-law indices (less than -5.1) than ours exterior to that point, whether it be a single power law (for the SW) or a broken power law (for the NE).

3.5.3. Disk Width

As part of the self-subtraction modeling process, we also extracted radial profiles for the disk projected FWHM, where the FWHM is measured from the pre-self-subtraction vertical profile model (g) at a given radial separation. We plot these radial profiles in Figure 7. In both bands, the disk FWHM consistently

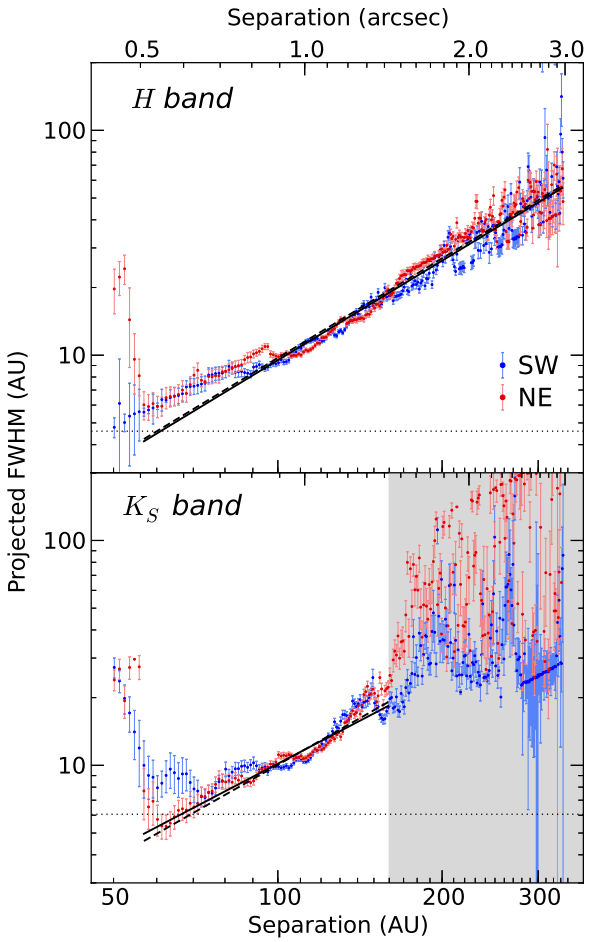

Figure 7. Projected FWHM of the pre-self-subtraction model disk as a function of separation for SW and NE ansae in H and K_s. We find the FWHM to generally increase with separation. The best-fit power-law functions are shown as solid lines for the SW and as dashed lines for the NE. The gray-shaded area in K_s marks the low-confidence region that we exclude from most of our results and discussion. The horizontal, dotted line indicates the diffraction limit ($1.22\lambda/D$) at each band's central wavelength. The error bars represent 1 σ uncertainty levels that include χ^2_ν scaling and uncertainties associated with our simplified disk model.

(A color version of this figure is available in the online journal.)

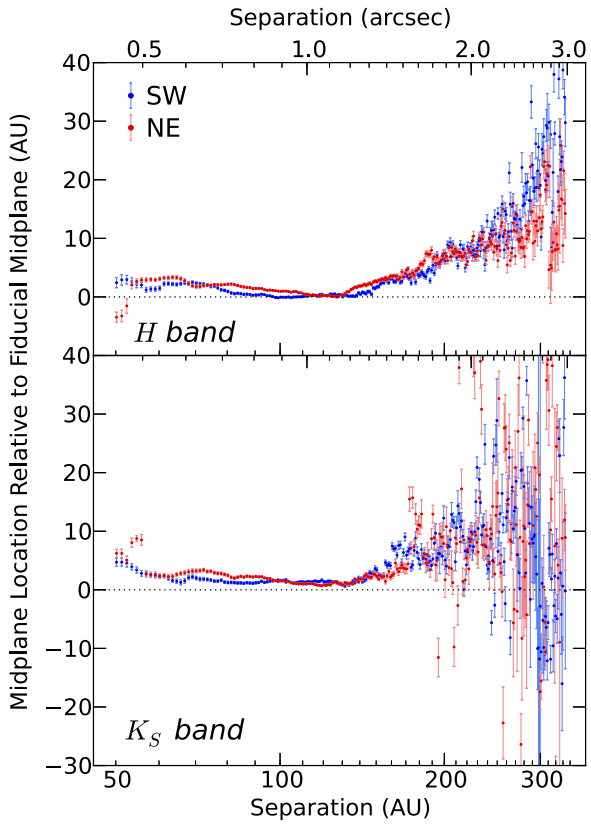

Figure 8. Disk midplane location measured by the self-subtraction modeling algorithm and relative to the fiducial midplane location (PA = 47°.5 east of north; dotted line) as a function of separation for SW and NE ansae in H and K_s. A positive location corresponds to a position northwest of the fiducial midplane as it extends from the star, and a negative location is southeast of the fiducial midplane. The profiles show considerable northwest curvature of the disk, particularly in H. The error bars represent 1 σ uncertainty levels that include χ^2_ν scaling and uncertainties associated with our simplified disk model.

(A color version of this figure is available in the online journal.)

increases with separation. The only region in which this does not hold is at $r \lesssim 60$ AU, where speckles contaminate the disk and make it appear unusually broad. Currie et al. (2012b) also found FWHM to increase with separation. Boccaletti et al. (2012) noted that the FWHM of the K_s ADI/LOCI-processed disk increased with separation and determined, as we do, that model disks that were not affected by self-subtraction had generally larger FWHMs than the processed data.

In H, the FWHM ranges from 5 to ~60 AU. In K_s, the FWHM ranges from 6 to ~22 AU (in the region r = 60–160 AU). At $r > 160$ AU, the low S/N in the K_s image severely affected the model-fitting algorithm, leading to disk models that were implausibly wide. That the error bars do not fully account for the scatter in this region is possible evidence that the errors remain underestimated as a result of systematics involved with our model choice. It could also indicate a violation of our assumption of a Gaussian distribution. Qualitatively, we find that our K_s FWHMs are generally smaller than those of Currie et al. (2012b) and greater than the observed LOCI-reduced FWHM measurements of Boccaletti et al. (2012) at a given separation. We find no highly significant differences in FWHM between ansae in either band, similarly to Currie et al. (2012b). Perhaps serendipitously, we see a bump in the K_s SW profile at $r \approx 67$ AU that corresponds to a similar bump from Currie et al. (2012b), though again the significance is low.

However, we do find the FWHM to be an average of 7% wider in K_s than in H at $r \approx 60$–160 AU. This may be a true difference in the disk's appearance in the two bands or it may be a result of our modeling, as we discuss in Sections 4.1 and 4.4.2. The drop to FWHM ≈ 38 AU in the K_s SW profile at $r > 275$ AU is due to the same artifact discussed in the previous subsection. Finally, we note that the FWHM is greater than or statistically consistent with the resolution threshold set by the diffraction limit at all separations.

We fitted single power laws to the FWHM profiles to further investigate the increase in disk width as a function of separation. For both bands, we fitted the profiles to a minimum separation of 57 AU because the FWHM is likely biased by speckles inward of there. We fitted the H-band profile to its outermost separation and truncated the K_s profile at r = 160 AU for fitting purposes to avoid the low-confidence region. We find best-fit power-law indices of 1.47 ± 0.04 for both ansae in H, 1.27 ± 0.14 for K_s SW, and 1.38 ± 0.11 for K_s NE.

3.5.4. Midplane Position

Figure 8 shows radial profiles for the disk midplane position relative to a fiducial midplane with P.A. = 47°.5 east of north.

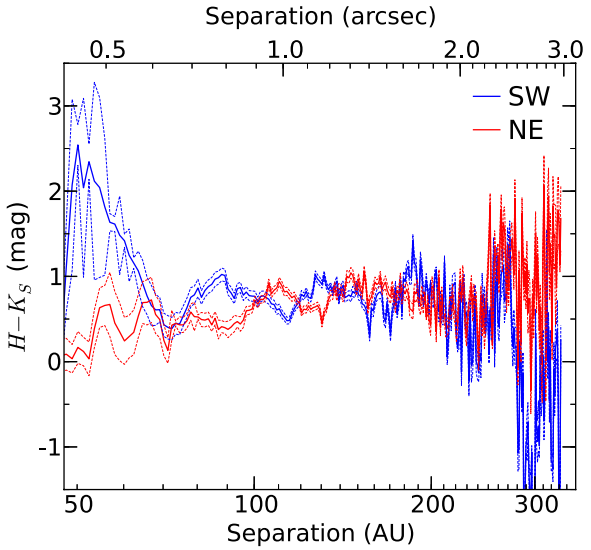

Figure 9. Disk $H-K_s$ color (solid lines) relative to the star as a function of radius, computed from self-subtraction-corrected one-dimensional brightness measurements. The SW ansa is in blue and the NE is in red. Dashed lines show the 1 σ confidence intervals, which include χ^2_ν scaling and uncertainties associated with our simplified disk model. The disk is generally red, and its color is approximately constant with r. We have lower confidence in our measurements at $r \gtrsim 160$ AU because of the low S/N in K_s in that region.

(A color version of this figure is available in the online journal.)

We locate this fiducial midplane based on visual inspection of our LOCI images and previous P.A. measurements (Debes et al. 2009; Boccaletti et al. 2012). We find that the midplane position moves farther toward the northwest as r increases, indicating bowing or curvature of the disk in that direction. This curvature begins to become more pronounced at $r \approx 130$ AU and is approximately equal in degree in both bands, with a maximum deviation of ~30 AU at the largest separations, although there is considerably more scatter in K_s at large separations, where S/N is low. We also find that the midplane most closely approaches the fiducial midplane at intermediate separations of $r \approx 80$–130 AU. Interior to this region, the midplane is again generally located farther to the northwest than the fiducial position.

Our results agree with previous reports of curvature in the disk. Boccaletti et al. (2012) reported a midplane deviation of a few AU to the north, particularly on the NE ansa in K_s, at $r \approx 67$–112 AU. This agrees approximately in amplitude and location with the nonzero deviation that we find for the midplane position of the inner disk. Northward curvature similar to the curvature we find in the outer disk was also noted by Currie et al. (2012b) at separations of $r \geqslant 100$ AU. Debes et al. (2009) reported westward curvature in the SW ansa (and suggested similar curvature in the NE ansa) at separations of 0.″5–3.″0, something that Boccaletti et al. (2012) also possibly detected. Previously, Kalas (2005) had noted that the SW disk emission curved west with radius at separations greater than 5.″0. We discuss possible causes of the curvature in Section 4.4.3.

3.5.5. Disk Color

Using the one-dimensional brightness profiles presented above, we computed the $H-K_s$ color of the disk, which is shown in Figure 9. We normalized the disk color by subtracting the corresponding stellar color ($H = 7.62$, $K = 7.59$, from the Two Micron All Sky Survey; Cutri et al. 2003). The disk is generally red, with $0 \lesssim H-K_s \lesssim 1$ mag at all separations. In the highest-confidence region of $r < 160$ AU, we do not detect any highly significant color difference between the two ansae, nor do we find the disk to be particularly red at any single separation.

The red color of the disk in our data is most consistent with results from Boccaletti et al. (2012) when compared with other works. Boccaletti et al. (2012) mentioned that the disk was dimmer in H than in K_s, and their surface brightness profiles (their Figure 6) showed $K_s > H$ throughout much of the disk, although often with low statistical significance. Our results are less consistent with the conclusions of Debes et al. (2009), who inferred colors from the dust's normalized scattering efficiency and found the disk to be generally gray in the inner regions and blue at the outer edges over a wavelength range of 1.1–2.1 μm, with the exception of a red zone along the SW ansa between 127 and 313 AU. As noted in Section 3.5.1, disagreement of our photometry results with those of Debes et al. (2009) could stem from multiple sources of uncertainty. At shorter wavelengths than we investigated, Kalas (2005) combined an extrapolated R-band profile (based on surface brightness measurements at $r > 5''$) with the 1.1 μm profiles to derive a blue color. Considering only total flux per ansa, Mawet et al. (2009) stated that the 1.1 μm/K_s fractional flux ratio (with 1.1 μm data from Schneider et al. 2005) was perhaps slightly blue, although statistically consistent with a gray color.

We made an alternative measurement of the disk color using the disk's peak brightness only (which is simply the best-fit value in mJy arcsec^{-2} of the model parameter b_0). By this method, we find a slightly blue color at most separations and gray at the rest, which agrees better with the Debes et al. (2009) colors than our integrated brightness results. See Section 4.4.4 for further discussion of the differences between our two color measurements.

As comparing color measurements between different data sets and analysis procedures can be difficult, we leave a more detailed comparison to future work.

4. DISCUSSION

4.1. Fidelity of Brightness Modeling

In applying our technique to these data, we are modeling two things: (1) the underlying brightness distribution of the disk and (2) the self-subtraction function. If we first show that we are modeling self-subtraction properly, then we can characterize the accuracy of our recovered brightness distributions.

We tested the ability of our algorithm to model self-subtraction on synthetic ADI data sets in which we knew the underlying disk brightness distribution exactly. We created synthetic brightness distributions based on various vertical profile forms including Gaussian, Lorentzian, and cubic spline functions. These underlying distributions then had one of three levels of noise added: no noise, Gaussian-distributed noise added to each pixel, or the actual stellar PSF and speckle pattern from the K_s data set. Each data set was processed in the same manner as the real data using LOCI with a range of N_δ-values, and then our self-subtraction modeling algorithm was applied.

As expected, for the cubic spline-based distribution we generally achieved a near-perfect recovery of the self-subtracted final image and also the original underlying brightness distribution, even for the data set with real speckle noise included. Our radial profiles for integrated brightness, FWHM, and midplane location generally agreed with the synthetic input disk's pre-self-subtraction values to within the 1 σ errors we calculated.

This reproduction of the self-subtraction is by construction, but it serves as a verification of our implementation. We also recovered the Gaussian- and Lorentzian-based distributions but with less accuracy, as our spline model generally underestimated the disk FWHM and overestimated the peak and integrated brightnesses by more than 1 σ. We found that this was largely due to the inability of the simple spline function to perfectly reproduce the forms of the Gaussian and Lorentzian functions. This is discussed further below. Overall, these tests demonstrated that we could accurately forward model the location and amplitude of self-subtraction in a LOCI-processed image, provided we have an accurate model of the pre-self-subtraction brightness distribution and the scene is constant across all images. Therefore, we conclude that we are modeling the self-subtraction function correctly.

That leaves us to characterize our ability to model the underlying brightness distribution of our observations. We find that our simple model does not have a sufficient number of parameters to capture all of the observed disk structure. This is most clearly visible in the K_s deviates shown in Figure 5(e), where there are deviates of more than $3\sigma_i$ at the location of the disk. We expect that the discrepancies between observations and the model brightness distribution indicate that the best-fit model vertical profile was inaccurate at some separations. This could be partly due to noise or PSF residuals in the data that contaminated the disk signal and altered its apparent structure. It is likely that the form we chose for the vertical profile model was too simple and incapable of reproducing the disk shape perfectly, as was the case with our Gaussian and Lorentzian synthetic disks. Recall that the shape of the profile was entirely determined by just two variables (b_0 and b_1). With a more complex disk model, we could produce a more precise reconstruction of the disk's brightness distribution. The model form is also a potential source of the relatively bright emission far from the midplane in the pre-self-subtraction models (K_s especially). With only one parameter controlling the brightness of the profile's wings, that brightness could be overestimated because much of the information about such extended emission is lost to self-subtraction. In addition, as our fake-disk tests indicated, our quoted errors may not accurately reflect the uncertainty in the radial profile measurements if the spline model cannot adequately reproduce the true disk shape. Possible solutions to these problems include adding more control points to the spline model or changing to a different functional form (i.e., not a monotonic spline) for the profile.

By applying our forward-modeling technique, we are able to reduce the error in recovering the disk brightness to levels lower than the scale previously set by errors from self-subtraction. Therefore, our ability to accurately recover the disk brightness distribution is improved after applying our technique. This is illustrated by a comparison between brightness measurements made by means of our modeling with those from aperture photometry in Section 4.3. We are also able to make more sensible comparisons between different sets of observations, such as our H and K_s data sets. These two data sets included different numbers of images and different amounts of angular rotation, making the effect of self-subtraction differ between them as well. Our self-subtraction modeling puts the final H and K_s images on more equal footing for comparison than they would be otherwise.

The simple modeling that we have done in this work serves primarily as a guide for the construction of more detailed models. Using the rough estimates of the disk parameters that we have derived here, we can construct a three-dimensional model of the dust distribution (left to a future work). From that, we can extract a two-dimensional scattered-light distribution, quickly compute the self-subtraction function for that distribution, and combine the two to form a model that can be compared with the LOCI image. We emphasize that computing the self-subtraction function does not require processing the new scattered-light model with LOCI. This saves on computation time compared with the disk injection and prereduction disk subtraction methods mentioned in Section 2, which require LOCI reductions for each new model. We also reiterate that model–data comparisons in the disk injection method incorporate twice as much speckle noise as the same comparisons in our method because the injected model disk is inserted into the observed data, whereas our model disk can be free of noise and still have self-subtraction applied to it.

4.2. Degeneracies in Brightness Modeling of ADI Data

We have seen that ADI and LOCI processing filters image data, as discussed in Section 1, with the degree of filtering dependent on the amount of field rotation in the data set and the aggressiveness of the PSF subtraction (which largely depends on the LOCI parameter N_δ). This filtering means we have incomplete information, from which we are trying to recover the disk brightness distribution. Consequently, recovery of that distribution's parameters from a single processed image will be degenerate. Such dependence on image processing methods is common among high-contrast imaging studies. However, we can reduce the degeneracy on some spatial scales by simultaneously fitting image data processed with different values of N_δ. This does require multiple LOCI reductions of the data, but we found just eight and nine reductions to be sufficient for H and K_s, respectively (Section 3.4). Plus, it is easy to compute the self-subtraction function for different reductions, as only N_δ and the LOCI coefficients change.

Fitting multiple reductions will not totally remove degeneracy, as the disk emission on the largest azimuthal scales will still be filtered out through ADI image processing. Nevertheless, this approach will help break degeneracy on the scales governed by N_δ.

4.3. Comparison with Aperture Photometry

The primary advantage of our modeled profiles is that they are corrected for self-subtraction, while aperture photometry makes measurements that are more strongly affected by self-subtraction.

Although aperture measurements are simpler to execute than our self-subtraction modeling method, the choice of aperture size has a large effect on results for an extended source. This is because self-subtraction varies according to both radial and azimuthal position in an image, and different sized apertures will probe different regions of the image. For example, a large aperture that extends beyond the disk and into the self-subtraction-generated negative-brightness regions will capture all of the disk light but also some of the negative brightness, thereby biasing the surface brightness measurements downward. A smaller aperture would yield different results. In addition, aperture photometry is sensitive to variations in disk width and the degree of self-subtraction with projected separation. In contrast, the modeled profiles are relatively immune to these factors. We attempted to quantify the effect of aperture size on the surface brightness profile for our highest-S/N H-band image in Figure 10.

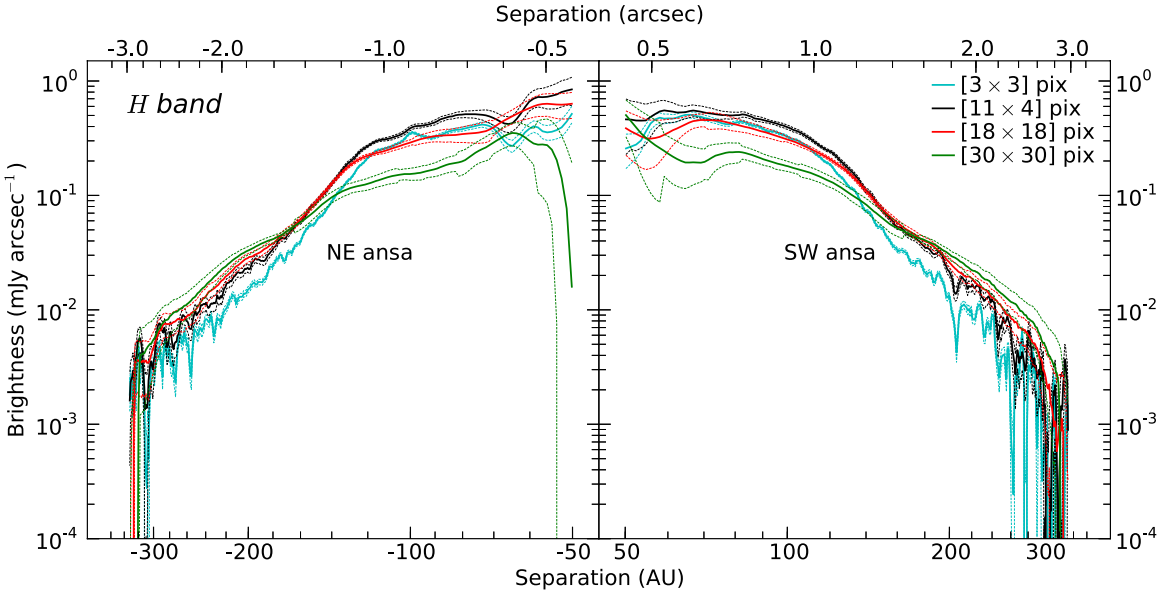

Figure 10. Aperture photometry brightness measurements converted to one-dimensional integrated brightness profiles (solid lines) for the *H*-band LOCI final image. Dashed lines show the 1 σ confidence intervals. Four different aperture sizes (azimuthal × radial diameter) were used: 3 × 3 (cyan), 11 × 4 (black), 18 × 18 (red), and 30 × 30 pixels (green). Brightness values for a given separation can vary between different-sized apertures by factors up to ∼2.5. The star is located at $x = 0$ (not plotted).

(A color version of this figure is available in the online journal.)

We calculated the mean surface brightness in rectangular apertures centered azimuthally on the fiducial midplane (see Section 3.5.4) and centered radially at each pixel from the star. The apertures were 11 × 4, 3 × 3, 18 × 18, and 30 × 30 pixels in dimension (azimuthal by radial diameter). The first size was our best guess at an aperture that would capture the maximum amount of disk flux and minimum negative brightness in the inner part of the disk, where we are most interested in the structure. The other sizes were chosen to be much smaller and much larger than our optimal choice. For an aperture of a given size, we determined a correction factor to account for the likelihood that some disk brightness falls outside of the finite aperture. The disk brightness apertures are allowed to overlap in the radial direction, so no correction factor is needed for that dimension. Therefore, we construct an aperture with the same azimuthal width as that used for the disk brightness measurements but with an infinite radial width and compute the correction factor as the ratio of the flux within that aperture centered on an unocculted reference star to the total flux of the reference star. This correction factor was then divided into all surface brightness measurements for the given aperture.

To estimate the uncertainty on a disk surface brightness measurement at a given radial separation, we placed nonoverlapping apertures in regions empty of disk brightness at the same radial separation and took the standard deviation of the mean surface brightnesses within those apertures. We then added this standard deviation term in quadrature with a Poisson photon-noise estimate to obtain the total uncertainty. The surface brightnesses and their associated uncertainties were converted to one-dimensional integrated brightnesses (mJy arcsec^{-1}) by integrating over the azimuthal dimension of the aperture for comparison with our model profiles.

As Figure 10 shows, the four different aperture sizes produced significantly different brightness profiles in *H*, even after correcting for finite aperture size. All four profiles show a general trend of decreasing brightness with increasing separation, with shallower slopes in the inner disk and steeper slopes in the outer disk. Overall, larger apertures show shallower slopes than smaller apertures in both the inner and outer disk. In terms of absolute brightness, the "optimal" 11 × 4 profile is brightest in the inner disk, the 30 × 30 profile is dimmest, and the other two fall in between. For the outer disk, the 30 × 30 profile is brightest, the 3 × 3 profile is dimmest, and the others fall between these two. We do not plot the K_s profiles but note that they show similar trends and discrepancies of the same order.

There are two effects related to aperture size that drive the differences between these profiles. First, smaller apertures fail to capture all of the flux from the disk, which biases the integrated brightness downward relative to larger apertures. This explains why the 3 × 3 profile is consistently below the other profiles in the outer disk. Second, the larger apertures encompass more of the negative brightness created by self-subtraction on either side of the midplane, thereby biasing the integrated brightness downward relative to smaller apertures. This explains why the 18 × 18 and 30 × 30 profiles are dimmer than the 11 × 4 profile in the inner disk, as the latter was chosen specifically to match the width of the disk in this region and not include negative brightness. The outer disk exhibits less negative brightness, so the larger apertures do not suffer as much from this effect there and tend to produce brighter profiles than smaller apertures do. The two effects appear to balance each other at intermediate separations for the 3 × 3 and 30 × 30 apertures, because their profiles show similar brightnesses at $r \approx 115$ AU.

In comparison with the *H*-band model profiles, the aperture profiles for all sizes are generally equal or lower in brightness for a given separation. The ratio of model brightness to the "optimal" *H* 11 × 4 aperture brightness is $\gtrsim$1 for all r (except at $r < 60$ AU, where the ratio is as low as ∼0.7 but the two profiles are statistically consistent) and predominantly between 1.5 and 7, with a possible trend of the ratio increasing with separation. When we compare the K_s model and aperture profiles, the model profiles are generally between two and eight times

brighter than the 11 × 4 aperture profiles. Consequently, in both ansae and both bands, we find that our modeling process produces brightness profiles equivalent to or brighter than profiles produced by a best-case aperture. This is evidence that our algorithm recovers brightness lost to self-subtraction, and though we may be biased by the use of the spline model, it does so without the uncertainties involved with selecting an appropriate aperture size.

Another factor to consider when measuring brightness is ease of comparison between data sets and studies. One-dimensional integrated brightness profiles are more straightforward to compare across different wavelengths, data sets, and implementations than are aperture photometry profiles. This is because the one-dimensional profiles are integrated along the azimuthal dimension, leaving room for uncertainty only in the treatment of the measurement in the radial direction. This is one less than the two dimensions that can vary in standard aperture photometry measurements. Even in the absence of self-subtraction, this advantage remains. There is also the additional advantage of a relationship between the one-dimensional integrated brightness and the vertical optical depth to scattering presented by the grains (Graham et al. 2007), which provides the opportunity to gain information about the latter quantity.

4.4. Model Structure of HD 32297

Our HD 32297 observations benefit from some of the highest angular resolution imaging of the system to date. They are a valuable addition to the existing library of observations for this system, as high-contrast imaging is inherently difficult and results are dependent on the instrument and techniques used. As discussed in Section 3.5.1, the various systematic errors involved with different types of observations and data analysis routines act as an incentive to measure the properties of this disk using multiple independent data sets. Here we discuss several implications of our results for the physical structure of the debris disk.

4.4.1. Brightness Profile Implications

Brightness asymmetries in debris disks can act as signposts of planets or collisions within the disk (e.g., Wyatt et al. 1999; Ozernoy et al. 2000). However, we do not believe that the asymmetries we see in our radial brightness profiles indicate the existence of either in this system. Although some of the asymmetries appear statistically significant, this is still largely a proof-of-concept test, and uncertainties in the systematics involved with high-contrast imaging and our disk modeling (such as artificially inflated FWHM) preclude us from drawing further conclusions. Overall, the general symmetry of the disk ansae could be the result of a relatively smooth dust distribution or it could be due to the fact that when an optically thin disk is viewed edge-on, a given projected separation averages over the dust density at many radial separations.

The breaks in the brightness profile power laws we reported are perhaps more informative. Similar breaks in brightness profiles from previous studies of HD 32297 (Debes et al. 2009; Boccaletti et al. 2012; Currie et al. 2012b) have been attributed to the presence of a planetesimal "birth ring" located at the break radius (Strubbe & Chiang 2006). Our measurements of the break point would locate the ring in the range 95 AU $\lesssim r \lesssim$ 125 AU. This is also consistent with the location of the cold dust ring estimated to be centered at 110 AU by Donaldson et al. (2013). Translation of our break location to a planetesimal ring radius requires modeling of the grain scattering phase function, which is beyond our current scope.

The differences between our ADI-corrected results and those from NICMOS observations are interesting, because both methods have distinct associated systematic uncertainties. We have already discussed some of the potential systematic errors involved with our observations and data analysis. *HST* observations by Schneider et al. (2005) and Debes et al. (2009) also have potential systematic errors, although different from ours. For example, a spectral mismatch between the PSF reference star and HD 32297 could lead to over- or undersubtraction of the stellar PSF, as could PSF variations caused by the telescope's "breathing" (Fraquelli et al. 2004). In addition, the thermal background from the telescope could bias the photometry, particularly at 2.05 μm, as Debes et al. (2009) do not mention performing sky subtraction as recommended for observations with $\lambda \gtrsim 1.7\,\mu$m (Viana et al. 2009). Registration errors between stacked images are another possible error source in coronagraphic observations. Each of these systematic errors could impact the NICMOS photometry and, therefore, affect asymmetries in radial brightness profiles or disk colors (see Section 3.5.5). Our brightness profiles agree more closely with previous ground-based results than with the *HST* results and do not settle the question which observational method provides more accurate information about disk. Instead, we suggest that further observations and more complete understanding of the errors associated with high-contrast imaging and related image processing techniques are needed in order to answer this question with greater certainty.

4.4.2. Implications of FWHM for Disk Shape and Self-subtraction Modeling

Our radial FWHM profiles show that the disk's projected width generally increases as r increases. Evidence for projected width increasing with separation has been found in the roughly edge-on disks of β Pic (Golimowski et al. 2006, and references therein), HD 15115 (Rodigas et al. 2012), and AU Mic (Graham et al. 2007). The indices of the best-fit power laws for our FWHM profiles were all between 1.27 and 1.47, which, for example, are slightly steeper than the indices ranging from 0.6 to 0.9 that Kalas & Jewitt (1995) found for the β Pic disk at separations of ∼130–330 AU. One exception to the trend of increasing width in our data is at $r < 60$ AU, where we see a rise in both H and K_s widths as r decreases. With residual speckle noise still contaminating the disk signal this close to the star, this feature is likely spurious. However, new observations or data reductions that provide a smaller inner working angle would allow us to investigate whether the disk continues to narrow closer to the star or whether some mechanism is causing the disk to "puff up" at separations less than 60 AU. Future extreme-AO instruments such as GPI and SPHERE promise to offer such capability and help answer these questions. Three-dimensional modeling of the disk would also allow us to ascertain the actual disk width rather than just the projected width.

In addition, we do not see any sharp features in the FWHM profile that are significant. Such a feature could conceivably indicate the gravitational perturbation of grain or parent-body orbits, but our measurements do not clearly indicate such a scenario.

The wider FWHM that we see in K_s compared with H could be due to differently distributed dust populations responsible for scattering the two wavelengths or another physical mechanism. On the other hand, it could be a sign that our model overestimated the FWHM in K_s or underestimated it in H. We

apply the same modeling method to both data sets, so it would be unexpected for one set of measurements to be systematically offset as a result of something in the fitting process, yet we cannot rule this out, because there may be systematics that are not fully understood. Consequently, we take the measurements at face value and refrain from further interpretation.

Comparison of our K_s FWHM measurement with previous works may provide more support for the effectiveness of our self-subtraction modeling algorithm. As noted in Section 3.5.3, our FWHM values for a given separation are generally smaller than the values reported by Currie et al. (2012b) and greater than those reported by Boccaletti et al. (2012). This is telling, because Currie et al. (2012b) used a conservative LOCI ($N_\delta \geqslant 2.5$, $W = 5.5$ AU) that would reduce self-subtraction, while Boccaletti et al. (2012) used a more aggressive LOCI (for the measurements in question; $N_\delta = 1.0$, $W = 7.3$ AU). We acknowledge that absolute comparisons between measurements from those works and our own are complicated by the different methods used. For example, the other works measured the FWHM of a Gaussian function fitted to the vertical profile, while we fitted a monotonic spline. Each work also included different corrections for self-subtraction in their measurements. Nevertheless, putting aside those issues and the complications of comparing reductions of different data sets with slightly different algorithms, it appears that our measurements fall between those taken from the aggressive and the conservative reductions. This implies that our self-subtraction modeling algorithm is able to recover the disk brightness above and below the midplane that is removed by LOCI.

4.4.3. Possible Sources of Disk Curvature

Our midplane position results showed a northward curvature that qualitatively matched previous publications and may be explained by existing hypotheses. One such hypothesis is that the HD 32297 system is interacting with the ISM. This could cause brightness asymmetries (Kalas 2005) or warping of the outer disk by several degrees (Debes et al. 2009). The estimated radial velocity of HD 32297 ($v \approx 20\,\mathrm{km\,s^{-1}}$) is similar to that measured for the ISM ($v \approx 24\,\mathrm{km\,s^{-1}}$; Redfield 2007), but HD 32297's proper motion is primarily to the south, which could potentially cause the disk's dust grains to be swept toward the north. However, this also depends on the proper motions of the ISM clouds, and little is known about individual clouds in this region.

An alternative explanation is that a combination of scattering phase function and disk inclination can produce an observed curvature in the scattered-light surface brightness (Kalas & Jewitt 1995). If the disk is a few degrees from being perfectly edge-on and the dust grains are primarily forward-scattering, then the near side of the disk (between us and the star) will appear brighter than the far side. This could account for the curvature we see toward the north if the near side of the disk is the south edge of the disk in our images. A similar explanation was proposed for the curvature observed in the HD 15115 debris disk (Rodigas et al. 2012). Currie et al. (2012b) modeled this scenario for HD 32297 and found that a disk containing highly forward-scattering grains can cause a brightness asymmetry between the near and far sides that is more pronounced at small separations, causing a change in the midplane P.A. and an apparent warping. Boccaletti et al. (2012) also surmised that anisotropic scattering leads one edge of the disk to appear brighter than the other. Highly porous grains are expected to be forward-scattering (Graham et al. 2007) and might be one explanation for this feature, as Donaldson et al. (2013) found that models of the outer disk that were composed of highly porous (90% porosity) and icy grains provided the best fit to the disk's SED.

A complete explanation of the curvature may require both mechanisms. The difference in the amount of forward-scattered light observed from the near and far sides of the disk is least in the outer regions of the disk because of our viewing geometry, so the inclination may have little effect there. However, interaction of disk grains with ISM dust grains is expected to be stronger farther from the star (Artymowicz & Clampin 1997), so an ISM interaction could produce curvature at the edges of the disk while inclination effects lead to curvature of the inner disk. We also note that the midplane curvature abruptly begins to increase just beyond the average break location of our brightness profile power laws, which may indicate that the same physical mechanism is responsible for both features.

4.4.4. Implications of Disk Color for Grain Properties

The color profiles derived from our one-dimensional (azimuthally integrated) brightness measurements indicate a generally red color for the disk (Figure 9). This may imply grain sizes that are a few times larger than the approximately micron-sized grains typically thought to be the main source of scattering. Donaldson et al. (2013) calculated the blowout size for the disk grains to be about 1 μm (assuming spherical, astrosilicate grains) and derived a minimum grain size of 2.1 μm from their best-fit SED model. Both of these values would be roughly consistent with the grain sizes implied by our color estimate.

Alternatively, one can compute the disk color based on peak brightness rather than integrated brightness. Our peak brightness measurement is also intrinsically corrected for self-subtraction, although self-subtraction is typically least influential near the midplane, where we assume the peak to occur. We find the peak brightness profiles for both ansae to be slightly brighter in H than K_s, leading to a peak color that is slightly blue at most separations and gray at the rest. This agrees with the colors found by Debes et al. (2009) and is consistent with the disk's being populated by micron- or submicron-sized grains that scatter 1.6 and 2.15 μm light with approximately the same efficiency.

The discrepancy between the two methods may be due to imprecision in the modeled disk FWHM measurement. As referred to in Section 3.5.3, the K_s FWHM is generally larger than the H FWHM at a given separation. This greater width increases the K_s integrated brightness relative to the H integrated brightness but does not affect the peak brightnesses. Thus, the disk appears red when considering the integrated brightness, but it appears blue or gray when considering only the peak brightness. This is a case where a more complex model of the disk vertical profile would allow us to gain a more precise understanding of the dust population. The color derived from the peak brightness is likely more reliable, because it is less sensitive to the model choice than is the integrated brightness color, but this has the disadvantage of only probing the dust at the midplane.

5. CONCLUSIONS

We have presented a novel technique for forward-modeling self-subtraction in ADI/LOCI-processed images of extended emission and applied it to near-infrared scattered-light imaging of the HD 32297 debris disk. Our method successfully reproduced the self-subtraction pattern in our H- and K_s-band LOCI images using a relatively simple model of the disk's vertical brightness profile, the LOCI parameters, and the P.A.s of the

images in the ADI data set. The result of the modeling process was a model of the disk's two-dimensional surface brightness that was not distorted by self-subtraction and provided an approximation of the scattered-light distribution prior to image processing. In the future, this self-subtraction modeling could be used in combination with other versions of ADI or LOCI, such as those that use iterative reference PSF subtractions, masks, or damped coefficients.

From the self-subtraction-corrected models, we extracted radial profiles for the one-dimensional integrated brightness, projected FWHM, and midplane location of the disk. The brightness profiles did not indicate any clear asymmetries or structures, but our power-law fits showed a break that supports the existence of a planetesimal birth ring at $r \approx 110$ AU. We also demonstrated that the model-derived profiles contained less uncertainty from location-dependent self-subtraction and variable disk width than profiles measured by means of aperture photometry. The FWHM profiles indicated a projected disk width that increases with separation from the star. Our measurements of midplane location showed curvature toward the northwest that confirms previous reports of similar features. This curvature may be a combination of a geometric observational effect linked to the disk's nearly edge-on inclination and interaction of the disk with the ISM. In addition, we found the disk's color to depend on our choice of model for the disk vertical profile, but we estimate the midplane color to be blue or gray at all separations.

Our self-subtraction modeling technique provides a two-dimensional model of the disk's scattered light that is a good starting point for building a three-dimensional model that can provide more information about grain size, grain composition, dust density, and disk morphology. The speed and accuracy with which we can compute the self-subtraction function using this method will also be extremely useful in future work that will compare more complex two-dimensional model images with ADI-processed observations. We hope to apply our technique to a more detailed investigation of this system and to ground-based high-contrast AO observations of other circumstellar disks, with the goal of learning more about the origins of planetary systems.

The authors thank the anonymous referee for helpful suggestions that improved this manuscript. This work was supported in part by University of California Lab Research Program 09-LR-01-118057-GRAJ, NSF grant AST-0909188, and NASA Origins grant 09-SSO09-0124. T. Esposito was supported by a UCLA graduate research fellowship for the duration of this work.

The data presented herein were obtained at the W. M. Keck Observatory, which is operated as a scientific partnership among the California Institute of Technology, the University of California, and the National Aeronautics and Space Administration. The Observatory was made possible by the generous financial support of the W. M. Keck Foundation. The authors wish to recognize and acknowledge the very significant cultural role and reverence that the summit of Mauna Kea has always had within the indigenous Hawaiian community. We are most fortunate to have the opportunity to conduct observations from this mountain.

Facility: Keck:II (NIRC2)

REFERENCES

Amara, A., & Quanz, S. P. 2012, MNRAS, 427, 948
Artymowicz, P., & Clampin, M. 1997, ApJ, 490, 863
Beuzit, J.-L., Feldt, M., Dohlen, K., et al. 2008, Proc. SPIE, 7014, 701418
Boccaletti, A., Augereau, J.-C., Lagrange, A.-M., et al. 2012, A&A, 544, A85
Bonnefoy, M., Boccaletti, A., Lagrange, A.-M., et al. 2013, A&A, 555, A107
Bonnefoy, M., Lagrange, A.-M., Boccaletti, A., et al. 2011, A&A, 528, L15
Brandt, T. D., McElwain, M. W., Turner, E. L., et al. 2013, ApJ, 764, 183
Buenzli, E., Thalmann, C., Vigan, A., et al. 2010, A&A, 524, L1
Carson, J., Thalmann, C., Janson, M., et al. 2013, ApJL, 763, L32
Currie, T., Debes, J., Rodigas, T. J., et al. 2012a, ApJL, 760, L32
Currie, T., Rodigas, T. J., Debes, J., et al. 2012b, ApJ, 757, 28
Currie, T., Thalmann, C., Matsumura, S., et al. 2011, ApJL, 736, L33
Cutri, R. M., Skrutskie, M. F., van Dyk, S., et al. 2003, yCat, 2246, 0
Debes, J. H., Weinberger, A. J., & Kuchner, M. J. 2009, ApJ, 702, 318
Delorme, P., Gagné, J., Girard, J. H., et al. 2013, A&A, 553, L5
Donaldson, J. K., Lebreton, J., Roberge, A., Augereau, J.-C., & Krivov, A. V. 2013, ApJ, 772, 17
Ertel, S., Wolf, S., & Rodmann, J. 2012, A&A, 544, A61
Fitzgerald, M. P., & Graham, J. R. 2006, ApJ, 637, 541
Fitzgerald, M. P., Kalas, P. G., & Graham, J. R. 2007, ApJ, 670, 557
Fraquelli, D. A., Schultz, A. B., Bushouse, H., Hart, H. M., & Vener, P. 2004, PASP, 116, 55
Galicher, R., Marois, C., Macintosh, B., Barman, T., & Konopacky, Q. 2011, ApJL, 739, L41
Golimowski, D. A., Ardila, D. R., Krist, J. E., et al. 2006, AJ, 131, 3109
Graham, J. R., Kalas, P. G., & Matthews, B. C. 2007, ApJ, 654, 595
Guyon, O., Martinache, F., Clergeon, C., et al. 2011, Proc. SPIE, 8149, 814908
Hawarden, T. G., Leggett, S. K., Letawsky, M. B., Ballantyne, D. R., & Casali, M. M. 2001, MNRAS, 325, 563
Heap, S. R., Lindler, D. J., Lanz, T. M., et al. 2000, ApJ, 539, 435
Kalas, P. 2005, ApJL, 635, L169
Kalas, P., Graham, J. R., Chiang, E., et al. 2008, Sci, 322, 1345
Kalas, P., Graham, J. R., & Clampin, M. 2005, Natur, 435, 1067
Kalas, P., & Jewitt, D. 1995, AJ, 110, 794
Kuhn, J. R., Potter, D., & Parise, B. 2001, ApJL, 553, L189
Lafrenière, D., Marois, C., Doyon, R., Nadeau, D., & Artigau, É. 2007, ApJ, 660, 770
Lagrange, A., Bonnefoy, M., Chauvin, G., et al. 2010, Sci, 329, 57
Lagrange, A.-M., Boccaletti, A., Milli, J., et al. 2012, A&A, 542, A40
Macintosh, B. A., Graham, J. R., Palmer, D. W., et al. 2008, Proc. SPIE, 7015, 701518
Maness, H. L., Fitzgerald, M. P., Paladini, R., et al. 2008, ApJL, 686, L25
Marois, C., Lafrenière, D., Doyon, R., Macintosh, B., & Nadeau, D. 2006, ApJ, 641, 556
Marois, C., Macintosh, B., Barman, T., et al. 2008, Sci, 322, 1348
Marois, C., Macintosh, B., & Véran, J.-P. 2010a, Proc. SPIE, 7736, 77361J
Marois, C., Zuckerman, B., Konopacky, Q. M., Macintosh, B., & Barman, T. 2010b, Natur, 468, 1080
Mawet, D., Serabyn, E., Stapelfeldt, K., & Crepp, J. 2009, ApJL, 702, L47
Milli, J., Mouillet, D., Lagrange, A.-M., et al. 2012, A&A, 545, A111
Moerchen, M. M., Telesco, C. M., De Buizer, J. M., Packham, C., & Radomski, J. T. 2007, ApJL, 666, L109
Mouillet, D., Larwood, J. D., Papaloizou, J. C. B., & Lagrange, A. M. 1997, MNRAS, 292, 896
Mueller, M., & Weigelt, G. 1987, A&A, 175, 312
Ozernoy, L. M., Gorkavyi, N. N., Mather, J. C., & Taidakova, T. A. 2000, ApJL, 537, L147
Perrin, M. D., Graham, J. R., Kalas, P., et al. 2004, Sci, 303, 1345
Perryman, M. A. C., Lindegren, L., Kovalevsky, J., et al. 1997, A&A, 323, L49
Persson, S. E., Murphy, D. C., Krzeminski, W., Roth, M., & Rieke, M. J. 1998, AJ, 116, 2475
Quanz, S. P., Amara, A., Meyer, M. R., et al. 2013, ApJL, 766, L1
Quanz, S. P., Schmid, H. M., Geissler, K., et al. 2011, ApJ, 738, 23
Quillen, A. C. 2006, MNRAS, 372, L14
Racine, R., Walker, G. A. H., Nadeau, D., Doyon, R., & Marois, C. 1999, PASP, 111, 587
Redfield, S. 2007, ApJL, 656, L97
Rodigas, T. J., Hinz, P. M., Leissenring, J., et al. 2012, ApJ, 752, 57
Schneider, G., Silverstone, M. D., & Hines, D. C. 2005, ApJL, 629, L117
Skemer, A. J., Hinz, P. M., Esposito, S., et al. 2012, ApJ, 753, 14
Smith, B. A., & Terrile, R. J. 1984, Sci, 226, 1421
Smith, W. H. 1987, PASP, 99, 1344
Soummer, R., Pueyo, L., & Larkin, J. 2012, ApJL, 755, L28
Strubbe, L. E., & Chiang, E. I. 2006, ApJ, 648, 652
Thalmann, C., Grady, C. A., Goto, M., et al. 2010, ApJL, 718, L87
Thalmann, C., Janson, M., Buenzli, E., et al. 2011, ApJL, 743, L6
Thalmann, C., Janson, M., Buenzli, E., et al. 2013, ApJL, 763, L29

Thebault, P., Kral, Q., & Ertel, S. 2012, A&A, 547, A92
Tokunaga, A. T., & Vacca, W. D. 2005, PASP, 117, 421
Viana, A., Wiklind, T., Koekemoer, A., et al. 2009, NICMOS Instrument Handbook, Version 11.0 (Baltimore, MD: STScI)
Vigan, A., Moutou, C., Langlois, M., et al. 2010, MNRAS, 407, 71
Wyatt, M. C. 2003, ApJ, 598, 1321
Wyatt, M. C. 2006, ApJ, 639, 1153
Wyatt, M. C. 2008, ARA&A, 46, 339
Wyatt, M. C., Dermott, S. F., Telesco, C. M., et al. 1999, ApJ, 527, 918
Yelda, S., Lu, J. R., Ghez, A. M., et al. 2010, ApJ, 725, 331